Synthesis, Characterization and Electrochemical Detection of Glucose and H₂O₂, Molecular Docking and Biological Inspection of Transition Metal Complexes of Novel Ligand 2-[(5-methyl-1,3-benzoxazol-2-yl)sulfanyl]acetohydrazide

Lubna Afroz [1] 🆔 **, Moodgere Habeebulla Moinuddin Khan** [1,*] 🆔 **, Hosadu Manjappa Vagdevi** [2] 🆔 **,**
Mohammed Shafeeulla Rasheed [2] 🆔 **, Malathesh Pari** [2] 🆔 **, Anjaiah Subbaraju** [2] 🆔

[1] Department of Chemistry, JNN College of Engineering, (VTU) Shivamogga-577204, Karnataka, India; lubna_noor88@yahoo.co.in (L.A.); drmk@jnnce.ac.in (M.H.M.K.);

[2] Department of Chemistry, Sahyadri Science College, Kuvempu University, Shivamogga-577203, Karnataka, India; vagdevihm17@gmail.com (H.M.V.); mdshafee14@gmail.com (R.M.S.); malathshpari@gmail.com (M.P.); subbu.hearty@gmail.com (A.S.);

* Correspondence: drmk@jnnce.ac.in (M.H.M.K.);

Abstract: A renowned pharmacophore and structure of great relevance to various fields, benzoxazole is a prominent member of the heterocyclic family. Aside from that, metal complexes can enhance the drug action and efficacy of the organic therapeutic agent. These insights led us to conduct research, including synthesizing and characterizing benzoxazole-derived ligand and metal complexes, assessing their pharmacological properties, and the potential use of the metal complex as a biosensor for sensing glucose and H₂O₂. The novel ligand MBA and its transition metal complexes are synthesized and characterized for their geometrical composition by varied physical and spectroscopic procedures. Antimicrobial potency was measured by the well diffusion method and antioxidant levels by the DPPH technique. A molecular docking study and MTTtest were carried out to assess anticancer activity for MCF-7 and Hela cell lines. The study results show that MBA bear bidentate coordination and octahedral geometry are ideal for the coordination of metals. The Co(II)MBA/GCE sensor demonstrated astounding electrochemical activity for glucose, and H₂O₂ and Ni(II) and Cu(II) compounds had impressive antimicrobial and cytotoxic potency, whereas Co(II) and Ni(II) complex were stronger antioxidant agents.

1. Introduction

Infectious diseases account for a large number of worldwide deaths. The chronic inflammation associated with these contagious diseases remains a compelling and demanding issue due to the higher prevalence of microbial pathogens that resist conventional antibiotics. Although combating pathogenic infections has advanced toward an expansive range of antibiotics and chemotherapeutic agents, there is still a substantial requisite to design a novel class of efficacious antimicrobial agents [1]. In addition, despite the phenomenal advances in

basic and clinical research that have resulted in distinctive cure rates for various malignancies, cancer persists as the second deadliest disease globally and the principal cause of death in developing and developed countries. However, cancer research has resulted in an assortment of novel and extremely potent treatments, yet the medications utilized to battle these diseases have clear restrictions. Subsequently, there is an earnest requirement for novel anticancer drugs with excessive adequacy, less harmful to non-cancerous cells, and explicit action targets [2, 3].

Presently, the predominance of coordination chemistry is being witnessed with the synthesis and evaluation of numerous transition metal complexes of heterocyclic ligands bearing nitrogen, oxygen, and sulfur donors. Further, these coordination compounds' priority doubles when the ligands and their metal complexes demonstrate noteworthy biological properties [4]. However, the progression of multicurative drugs using coordination compounds, specifically the complexes of heterocyclic moieties, has invariably been a crucial area of research in bio-inorganic and medicinal chemistry. The utilization of metal-based drugs to treat numerous infections not only cures certain diseases but conjointly diminishes the high toxicity and further guides to acknowledge the various mechanistic pathways to regulate the clinical issues. In light of this, scientists across the globe are working more intensively on designing metal-based drugs with heterocyclic ligand systems [5].

Among the heterocyclic family, benzoxazole, the most reputed planar aromatic heterocycle, is a vital pharmacophore and an extremely advantageous structure in medicinal chemistry. Benzoxazole is an organic compound in which benzene is conjugated with an oxazole ring. Oxazole is a 1,3 azole with one oxygen atom and one nitrogen atom of pyridine type at the 3-position in the five-membered ring [6]. Additionally, benzoxazole and its analogs show off an exciting range of biological and pharmacology like antimicrobial, antifungal, antitumor, antibiotic, and topoisomerase I and II inhibitors [7, 8]. On top of that, benzoxazole derivatives are likewise employed as building blocks for biochemical and pharmaceutical products and other industrial applications, including dyes, fluorescent bleaches, and biomarkers or biosensors. Aside from their biological significance, a wide array of transition metal ions can be stably complexed with benzoxazole-derived ligands [9].

In a healthy human body, normal blood sugar level is found between 4.9-6.9 mM and elevation in glucose levels over an extended time leads to diabetes. Diabetes is a prolonged and incurable disease globally, leading to an enormous number of deaths yearly. On the other hand, hydrogen peroxide (H_2O_2) is broadly used in environmental, drug, clinical and industrial research. It is a by-product of reactions catalyzed by an immense number of oxidase proteins and performs a crucial role in forming extremely reactive and exceedingly toxic hydroxyl radicals. It is possible to contract life-threatening diseases such as cancer and cardiovascular issues by exceeding the usual concentration of hydrogen peroxide [10, 11]. While countless techniques are available to detect the aforementioned molecules, electrochemical methods are widely accepted because of their high affectability, ease of use, minimal size, and investment. One of the above methods is Cyclic voltammetry (CV), a potentiodynamic electrochemical procedure for examining electroactive species which measures the current flowing through an electrode by continuously cycling the potential along a linear path. Carbon-based electrodes are often utilized as working electrodes in CV methods due to their diverse structures and suitability across many potential ranges. A glassy carbon electrode (GCE) is a frequently considered carbon-based electrode for the electrochemical analysis of oxidizable compounds. Besides being electrochemically stable, GCE is chemically inert, has a lesser gas permeability, has better biocompatibility, and has a very small thermal expansion coefficient [12, 13]. In the

current study, a modified Co(II) metal complex is used to rapidly sense glucose and hydrogen peroxide.

As far as we are aware, there exists no study that has illustrated the physicochemical characterization, electrochemical studies of glucose, hydrogen peroxide, and biological investigation of 3d metal (II) complexes of ligand 2-[(5-methyl-1,3-benzoxazol-2-yl)sulfanyl]acetohydrazide (MBA). Besides the obvious essentiality of new restorative medications for cancer treatment, metal complexes of the ligand were additionally tried for their potency on two distinct cancer strains. Hence, the above comprehensive facts lead to the present work, which aims to synthesize novel ligand 2-[(5-methyl-1,3-benzoxazol-2-yl)sulfanyl]acetohydrazide (MBA) and its transition metal complexes which are characterized by various spectral methodologies, P-XRD, SEM analysis, CV method, and thermogravimetric studies. To date, the biological effects induced by d-block metal complexes of MBA have not been performed or cited. Thus this paper also focused on determining the biological efficacy of transition metal complexes of ligand MBA, which could discover its implementation in metal-based chemotherapy/pharmacology as antimicrobial, antioxidant, and cytotoxic agents. As part of the docking study, the binding affinity of the ligand and its metal complexes with target proteins was explored.

2. Materials and Methods

2.1. Resources and instrumentation.

Each of the particular starting materials, reagents, and solvents utilized in this study were refined and of AR grade. 2-Amino-4-methyl phenol, Carbon disulfide, Ethyl chloroacetate, Hydrazine hydrate, and all the metal salts were sourced from Sigma-Aldrich, Hi-Media, and no further purification was required. Melting points were noted on digital melting point apparatus SMP 30 Stuart, UK. ^{1}H and ^{13}C NMR spectra were recorded at the Centralized Instrumentation Facility, Mysore University, Karnataka, India. The chemical shifts are described in δ values (ppm) using tetramethylsilane (TMS) as an internal standard. By LC-MS spectroscopy, molecular weights of synthetic compounds were characterized via Shimadzu GCMSQP2010S mass spectrometer. Elemental analysis (C, H, and N) were assessed by the Vario-Micro Qub elemental analyzer. Through the aid of the Parkin Elmer spectrophotometer, infrared spectra were recorded with KBr pellets at 250 - 4000cm^{-1}. Magnetic susceptibilities were identified at room temperature through the Gouy method. Molar conductance measurements were completed utilizing the solution of the metal complexes in DMF (10^{-3}) through an Equip-Tronics EQ-660A conductivity meter. X-ray Diffractometer (Rigaku Miniflex 600,5th gen) with Cu-K$_\alpha$ radiation (wavelength 0.154nm), Systronics UV–VIS spectrometer-119 was utilized, and TGA analysis of metal complexes was expected by SDT Q600 V20.9 Build 20 from the room temperature to 850°C in a nitrogen atmosphere (20mL min^{-1}) and below the heating pace of 20°C min^{-1} at SAIF, Karnataka University, Dharwad. Electrochemical experiments were concluded by CH-instruments, Electrochemical analyzer CHI608D, USA, at JNN College of Engineering, Shimoga. The surface morphology of the synthesized compounds was deduced via a Zeiss scanning electron microscope.

2.2. Synthesis of ligand 2-[(4-methyl-1,3-benzoxazol-2-yl)sulfanyl]acetohydrazide (MBA).

The synthesis of ligand 4-[(6-methyl-1,3-benzoxazol-2-yl)sulfanyl]acetohydrazide(MBA) is comprised of three steps. The intermediates **a, b,** and the

final product **c** (MBA) ligand were synthesized using the literature methods [14, 15]. The reaction pathway is highlighted in Figure 1.

2.2.1. Synthesis of 4-methyl-1,3-benzoxazole-2-thiol (a).

To begin with, in an round-bottomed flask, potassium hydroxide (1.1eq) was dissolved thoroughly in methanol (50 ml) by stirring for 15mins accompanied by the gradual addition of an estimated amount of carbon disulfide (1.5eq) at room temperature. As a next step,2- Amino-4-methyl phenol (1eq) was added to the formerly mentioned reaction mixture, which was again well stirred for 10min and refluxed for approximately 6hrs in a water bath. The completion of the reaction was ensured via TLC (Ethyl acetate : Petroleum ether, 1:2). After the reaction was completed, the solution was transferred to a beaker consisting of ice water and acidified with glacial acetic acid. The separated brown precipitate was washed multiple times with water, filtered, dried, and recrystallized [14]. Brown solid, Yield 95%. LC-MS mass (C_8H_7NOS)= 166.03 (M+1).

2.2.2. Synthesis of ethyl [(4-methyl-1,3-benzoxazol-2-yl)sulfanyl]acetate (b).

A weighed quantity of anhydrous potassium carbonate (1.2 eq) was dissolved entirely in acetone (20 ml) in around-bottomed flask via stirring for almost 15mins. An additional 4-methyl-1,3-benzoxazole-2-thiol (1 eq) was added to the earlier referenced reaction mass with consistent stirring for a few more minutes. After that, ethyl chloro acetate (1.5 eq) was added steadily to the above reaction mixture and refluxed in a water bath for 6 hrs. The completion of the reaction was affirmed by TLC (Ethyl acetate : Petroleum ether, 1:2). The resultant compound was added to the beaker filled with ice-cold water. The obtained pale brown precipitate was filtered and washed with water. After completely drying the resultant product, the glittery pale brown crystalline residue was achieved, which was recrystallized from methanol [15]. Light brown solid, Yield 89%. LC-MS mass ($C_{12}H_{13}NO_3S$) = 252.02 (M+1).

2.2.3. Synthesis of 2-[(4-methyl-1,3-benzoxazol-2-yl)sulfanyl]acetohydrazide (MBA) (c).

In the beginning, ethyl [(4-methyl-1,3-benzoxazol-2-yl)sulfanyl]acetate (1 eq) was stirred ina 25ml of methanol for 20 mins, followed by the addition of hydrazine hydrate (3 eq) to the aforementioned reaction mixture which was further stirred for 7 hrs at ambient temperature to gain the expected product. The completion of the reaction was ascertained by TLC (Chloroform:Methanol, 1:3). The retrieved creamy white product was filtered off and washed with pet ether. Later the compound was gathered after drying.

Data of ligand (MBA): Colourless solid, Yield: 85%, M.P. 159°C-162°C,IR (cm^{-1}): 3414 (v -NH$_2$),3302 (v -NH), 3048 (v Ar CH), 1648 (v C=O), 1534 (v C=N), 685 (v C-S-C); ^{1}H NMR (DMSO-d6)ppm: δ9.39 (bs, 1H, NH), δ7.09-7.49 (m, Ar-3H, benzene), δ4.32 (s, 2H, CH$_2$), δ4.02-4.03 (d, 2H,NH$_2$), δ2.37 (s, 3H, CH$_3$) ; LC-MS found (Calculated) for ($C_{10}H_{11}N_3O_2S$) = 238.06 (M+1) (237.27).
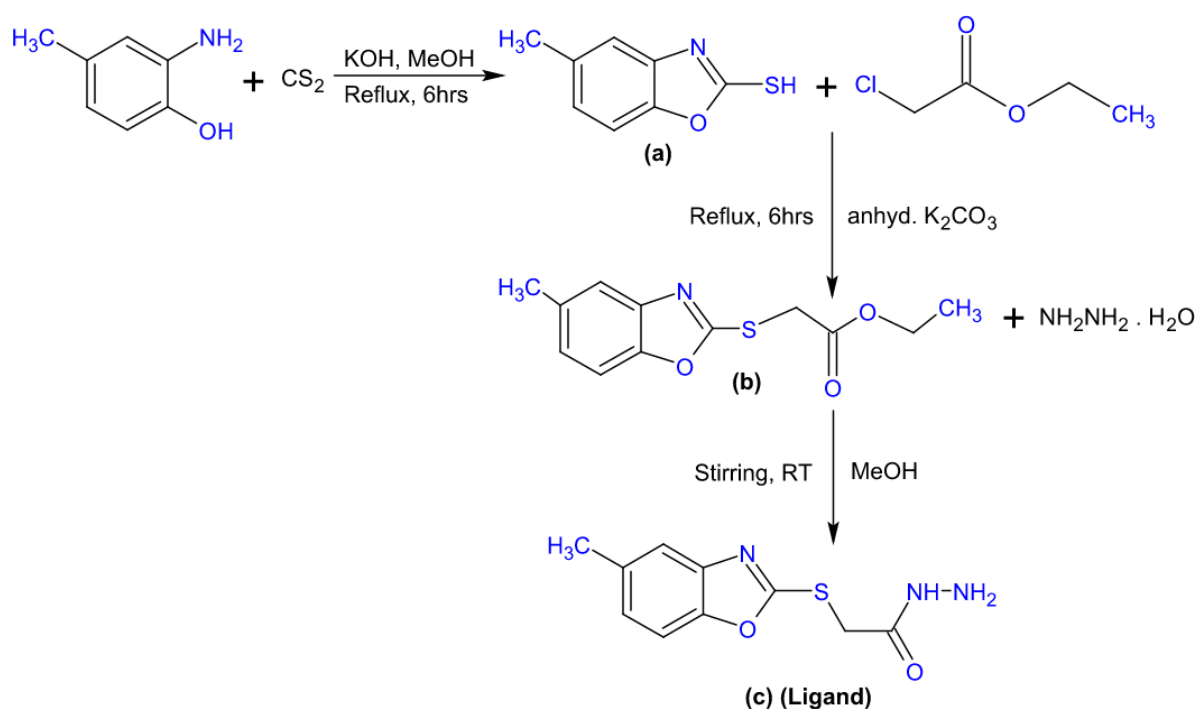
Figure 1. Synthesis of Ligand2-[(4-methyl-1,3-benzoxazol-2yl)sulfanyl]acetohydrazide(MBA):(**a**) 4- methyl-1,3-benzoxazole-2-thiol;(**b**) ethyl [(4-methyl-1,3-benzoxazol-2-yl)sulfanyl]acetate;(**c**) MBA.

2.3. Metal complex synthesis: a general procedure.

Chlorides of metal dissolved in warm ethanol (0.001 moles) $MCl_2.6H_2O$ (Co, Ni, Cu, Zn)were added in droplets to the hot ethanol solution of ligand MBA (0.002 moles) with continual stirring. Further stirring and refluxing of the resultant mixture was performed on a water bath for 6hrs, and once the reaction was completed, the final product was left to cool at room temperature. Precipitates of different colors were formed, which were later collected by filtration and washed with distilled water and cold ethanol before being dried in a vacuum desiccator over anhydrous calcium chloride. The synthesis and propounded structure of metal complexes are outlined in Figure 2.

2.3.1. [Co(MBA)$_2$.Cl$_2$] complex.

Light brown solid, Yield: 59%, M.P. 127°C-129°C, Elemental analysis (%) found (Calculated)for $C_{20}H_{22}O_4Cl_2N_6S_2Co$: C-39.46(39.70), H-3.17(3.64), N-13.28(13.89), Co-9.20(9.75); IR (cm^{-1}):3421 (v -NH$_2$), 3308 (v -NH), 3050 (v Ar CH), 1576 (v C=O), 1509 (v C=N), 689 (v C-S-C), 571(v M-O), 498 (v M-N); LC-MS found (Calculated) for $(C_{20}H_{22}O_4Cl_2N_6S_2Co)$ = 605.02 (M+1)(604.39); UV-vis: λ_{max} (nm): 613, 681; Conductance (Ω^{-1} cm^2 mol^{-1}): 15.

2.3.2. [Ni(MBA)$_2$.Cl$_2$] complex.

Wine red solid, Yield: 57%, M.P. 127°C-130°C, Elemental analysis (%) found (Calculated)for $C_{20}H_{22}O_4Cl_2N_6S_2Ni$: C-39.44(39.72), H-3.23(3.64), N-13.32(13.90), Ni-9.28(9.71); IR(cm^{-1}): 3424 (v -NH$_2$), 3307 (v -NH), 3046 (v Ar CH), 1580 (v C=O), 1511 (v C=N), 687 (v C-S-C), 573(v M-O), 494 (v M-N); LC-MS found (Calculated) for $(C_{20}H_{22}O_4Cl_2N_6S_2Ni)$ = 605.19 (M+1)(604.15); UV-vis: λ_{max} (nm): 429, 515; Conductance (Ω^{-1} cm^2 mol^{-1}): 12.

2.3.3. [Cu(MBA)$_2$.Cl$_2$] complex.

Dark brown solid, Yield: 61%, M.P. 267°C-269°C, Elemental analysis(%) found (Calculated)for C$_{20}$H$_{22}$O$_4$Cl$_2$N$_6$S$_2$Cu: C-39.32(39.40), H-3.34(3.61), N-13.52(13.79), Cu-10.18(10.43); IR(cm^{-1}): 3419 (υ -NH$_2$), 3310 (υ -NH), 3051 (υ Ar CH), 1579 (υ C=O), 1507 (υ C=N), 687 (υ C-S-C),576 (υ M-O), 497 (υ M-N); LC-MS found (Calculated) for (C$_{20}$H$_{22}$O$_4$Cl$_2$N$_6$S$_2$Cu) = 609.38(609.00); UV-vis: λ$_{max}$ (nm): 472, 575; Conductance (Ω^{-1} cm^2 mol^{-1}): 18.

2.3.4. [Zn(MBA)$_2$.Cl$_2$] complex.

Creamy white solid, Yield: 60%, M.P. 273°C-275°C, Elemental analysis (%) found(Calculated) for C$_{20}$H$_{22}$O$_4$Cl$_2$N$_6$S$_2$Zn: C-39.22(39.34), H-3.14(3.60), N-13.59(13.77), Zn-10.28(10.71); IR (cm^{-1}): 3417 (υ -NH$_2$), 3312 (υ -NH), 3051 (υ Ar CH), 1576 (υ C=O), 1504 (υ C=N),690 (υ C-S-C), 575 (υ M-O), 496 (υ M-N); LC-MS found (Calculated) for (C$_{20}$H$_{22}$O$_4$Cl$_2$N$_6$S$_2$Zn) =611.15 (M+1) (610.00); Conductance (Ω^{-1} cm^2 mol^{-1}): 16.
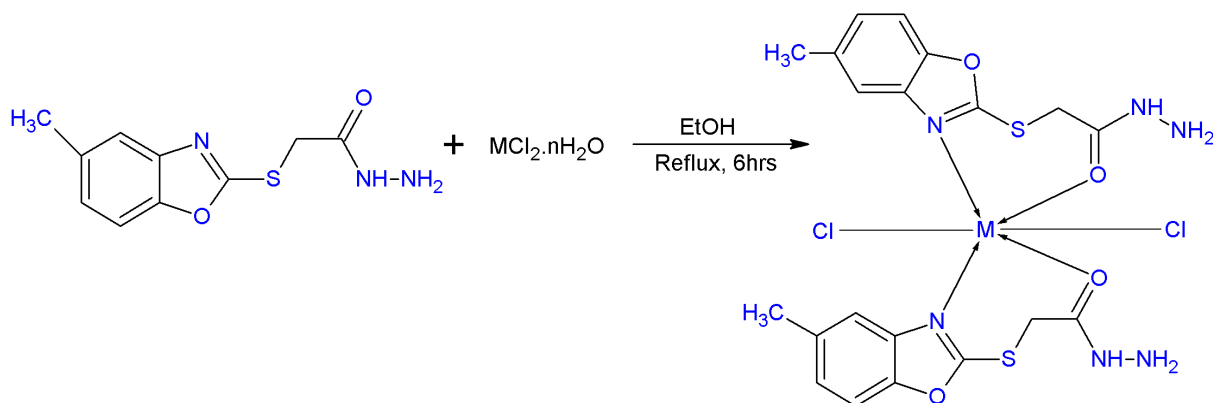

Figure 2. Synthesis and proposed structure of metal complexes(M = Co, Ni, Cu, and Zn).

2.4. Electrochemistry.

Experimental electrochemistry was performed with a prevailing three-electrode setup incorporating a glassy carbon electrode (GCE) as a working electrode, platinum wire as a counter, andAg/AgCl as a reference electrode. The electrode modification was achieved by using the drop-dry method. The surface of the glassy carbon electrode was cleansed evenly by polishing it with a fine aqueous slurry of alumina powder (0.3 and 0.05 mm) for nearly 5 mins. To eliminate residues of alumina particles, the electrode was wholly washed with deionized water followed by absolute ethanol and dried at room temperature. In the last, prepared Co(II) complex suspension was deliberately dropped on the cleansed GCE. The electrocatalytic activity of the Co(II) complex was tested by cyclic voltammeter using modified GCE towards varied concentrations of glucose andH$_2$O$_2$.

2.5. Antimicrobial activity.

2.5.1. Antibacterial screening.

An *in vitro* antibacterial study was done on MBA. Its coordinated metal compounds against four bacterial strains are *Staphylococcus aureus, Escherichia coli* (Gram-negative bacteria), *Bacillus subtilis,* and *Salmonella Typhi* (Grampositive bacteria) via agar well diffusion method. As part of the test, 24-old Muller-Hinton broth cultures of test bacteria were

dabbed on sterile Muller-Hinton agar plates with sterile cotton swabs, followed by puncturing 9mm holes with a sterile cork borer. To ensure consistency, Chloramphenicol drug as standard at two varied concentrations (100 and 200 µg/mL in 10% DMSO) and control (10% DMSO) was added to each well on an individual basis. Having stood for nearly 30 mins, the plates were oriented upright and incubated for 24 hrs at 37ºC [16]. Using vernier calipers, zone of inhibition was detected by observing the test solution as it diffused over time.

2.5.2. Antifungal screening.

An *invitro* antifungal test was performed via the Sabouraud dextrose agar diffusion method against *Candida albicans* and *Aspergillus niger* to verify the efficacy of MBA and its transition metal complexes [16]. The drilling of wells (9 mm in diameter) was done with a sterile cork borer, and the standard drug (Fluconazole, 100 µg/mL of sterile distilled water) and control (10% DMSO)were added to the wells that had been marked. The wells were filled with 140 µL from each (100 and200 µg/mL in 10% DMSO) of the test stock solution of compounds, and the plates were let to stand for an hour to accelerate diffusion. After 48 hrs of incubation at 37°C, the diameter of the zone of inhibition surrounding the wells was assessed via vernier calipers.

2.6. Minimum Inhibitory Concentration (MIC).

A minimum inhibitory concentration (MIC) assay is implemented to examine the least concentration of an antimicrobial agent that restrains the noticeable proliferation of a microorganism. The MIC of the uncoordinated ligand and its metallic compounds was tested by serial dilution. In this study, MBA and its metal complexes were administered to two bacterial and fungal strains at different concentrations of 100, 50, 25, and 12.5 mg/ml. The data received by the MIC studies are included in Tables 10(a) and 10(b).

2.7. Antioxidant activity.

The antioxidative capacity of MBA and its transition metal complexes was accomplished using the DPPH method as per published literature [17,18]. Compounds of diverse concentrations being dissolved in methanol were later injected into vials with a volume of 5 mL each. A 3 mL solution of 0.004% DPPH in methanol was transferred to each of these test vials, and for 30 minutes, themixtures were incubated at a convenient temperature with ascorbic acid as the standard. If DPPH abstracts hydrogen radicals from an external source, the absorption subsides stoichiometrically in relation to the number of electrons or hydrogen atoms. By using the subsequent equation, DPPH scavenging activity is evaluated, and absorbance was confirmed at 517 nm. In Table 11, the collected data are indexed accordingly.

$$\text{Scavenging ratio (\%)} = [(A_i - A_o) / (A_c - A_o)] \times 100\%$$

where, A_i represents the absorbance while the existence of a test compound, A_o represents the amount of absorbance of a blank in the absence of a test compound, A_c refers to the absorbance without the test compound.

2.8. Analysis of molecular docking.

The role of molecular docking is viewed as a powerful supportive tool in comprehending the degree of interaction of compounds with receptor sites. Molecular docking for the synthesized compounds was accomplished following the referenced procedure [19].

With the aid of Hexmolecular modeling package version 8.2, the three-dimensional crystal structure of epidermal growth factor receptor (EGFR) tyrosine kinase domain PDB code: 2A91 was used all through the work. Upon reorienting the ligand to 2D and 3D energy-minimized conformations using Hex 3DUltra 8.2, the conformations were visualized with the Acceryl Discovery Studio 3.1 Client. The *in-silico* molecular docking was determined on the anticancer receptor of PDB code: 2A91 using actinoin as the standard for docking studies. The crystal structure of the receptor was retrieved from the protein data bank, and all the water molecules and heteroatoms were evicted prior to screening for docking studies. Additionally, the docking values from Table 12 triggered our curiosity about carrying out a wet cytotoxicity analysis.

2.9. Anticancer activity [Cell culture and viability].

The *invitro* anticancer activity of MBA and its metallic complexes were evaluated using 3-(4,5-dimethythiazol-2- yl)-2,5-diphenyl tetrazolium bromide (MTT) assay against two human cancer cell lines MCF-7 (breast cancer) and HeLa (cervical cancer) [20]. The assay relied unconditionally on the reduction of tetrazolium salt by the mitochondrial dehydrogenase of viable cells to form a blue formazan product dissolved in DMSO and measured at 570 nm. Using graph Pad Prism Version 5.1, IC_{50} (µM) values of compounds were figured, and Paclitaxel was used as a positive control. National Centre for Cell Science, Pune provided human cancer cell lines, and the cells were cultured in Dulbecco's Modified Eagle Medium (DMEM) with low glucose (CatNo-11965-092, Gibco, Invitrogen) supplemented with 10% fetal bovine serum and 1% antimycotic(Cat No-15240062, Thermofisher Scientific) was also used for cell cultivation. The cells were seeded onto a 96-well flat bottom microplate and maintained overnight at 37°C, with 95% moistness and 5% CO_2. Varying concentrations (400, 200, 100, 50, 25, 12.5 µg/ml) of the sample were treated, and cells were incubated for another 48 hrs. After two thorough washes in PBS, wells were filled with 20 µL of MTT staining solution, and the plate was incubated at 37ºC for 20 minutes. As soon as the formazan crystals dissolved after adding 100 µL of DMSO to a particular well, the absorbance was read with a microplate reader at 570 nm after 4 hrs. The cytotoxicity effect was calculated using the beneath specified equations:

Cytotoxicity (%) = 1 – (Mean absorbance of test compound / Mean absorbance of –ve control) X100

Cell viability % = 100 – Cytotoxicity %

3. Results and Discussion

3.1. Chemistry.

The ligand MBA is a final product of intermediates 4-methyl-1,3-benzoxazole-2-thiol and ethyl [(4-methyl-1,3-benzoxazol-2-yl)sulfanyl]acetate, as presented in Figure 1. Observations have revealed that the MBA and it's newly synthesized coordinated compounds are stable in atmospheric conditions, entirely dissolvable in polar organic solvents, and moderately solubilized in common organic solvents. The analytical and physical data of MBA and its metal complexes are listed in Table 1. According to the analysis data, the proportion of ligand to metals in all the metal complexes was 1:2. A concentration of 0.001 M DMF solution of all the metal complexes was used to determine their molar conductance values at room

temperature. Typically all metal complexes in this study were measured to have conductance values of 12-18 $\Omega^{-1}cm^2mol^{-1}$, which validated their non-electrolytic character.

Table 1. Physical and analytical data of ligand and its metal complexes.

| Compounds | Mol. wt | % yield | CHN % Analysis found (calculated) | | | | Molar conductance (Ω^{-1} cm^2 mol^{-1}) | M.P. (°C) |
			M	C	N	H		
$C_{10}H_{11}N_3O_2S$ (MBA) Colourless	237.27	85	-	50.13 (50.57)	17.34 (17.70)	4.24 (4.63)	-	159-162
[Co(MBA)$_2$.Cl$_2$] Light brown	604.39	59	9.20	39.46 (39.70)	13.28 (13.89)	3.17 (3.64)	15	127-129
[Ni(MBA)$_2$.Cl$_2$] Wine red	604.15	57	9.28	39.44 (39.72)	13.32 (13.90)	3.23 (3.64)	12	127-130
[Cu(MBA)$_2$.Cl$_2$] Dark brown	609.00	61	10.18	39.32 (39.40)	13.52 (13.79)	3.34 (3.61)	18	267-269
[Zn(MBA)$_2$.Cl$_2$] Creamy white	610.00	60	10.28	39.22 (39.34)	13.59 (13.77)	3.14 (3.60)	16	273-275

3.2. ^1H NMR and ^{13}C NMR spectral studies.

The ligand MBA showed off a broad singlet at 9.39 ppm for –NH proton (bs, 1H, NH), and the other peaks obtained between 7.09-7.49 ppm were described as the aromatic protons of the benzene ring (m, Ar-3H, benzene). Further, a singlet was observed at 4.32 ppm corresponding to –CH proton(s, 2H, CH$_2$), while a doublet was spotted in the range 4.02-4.03, attributing to the presence of –NH$_2$protons (d, 2H, NH2) and finally, a singlet procured at 2.37 ppm was ascribed to the proton of a methyl group (s, 3H, CH$_3$) respectively.
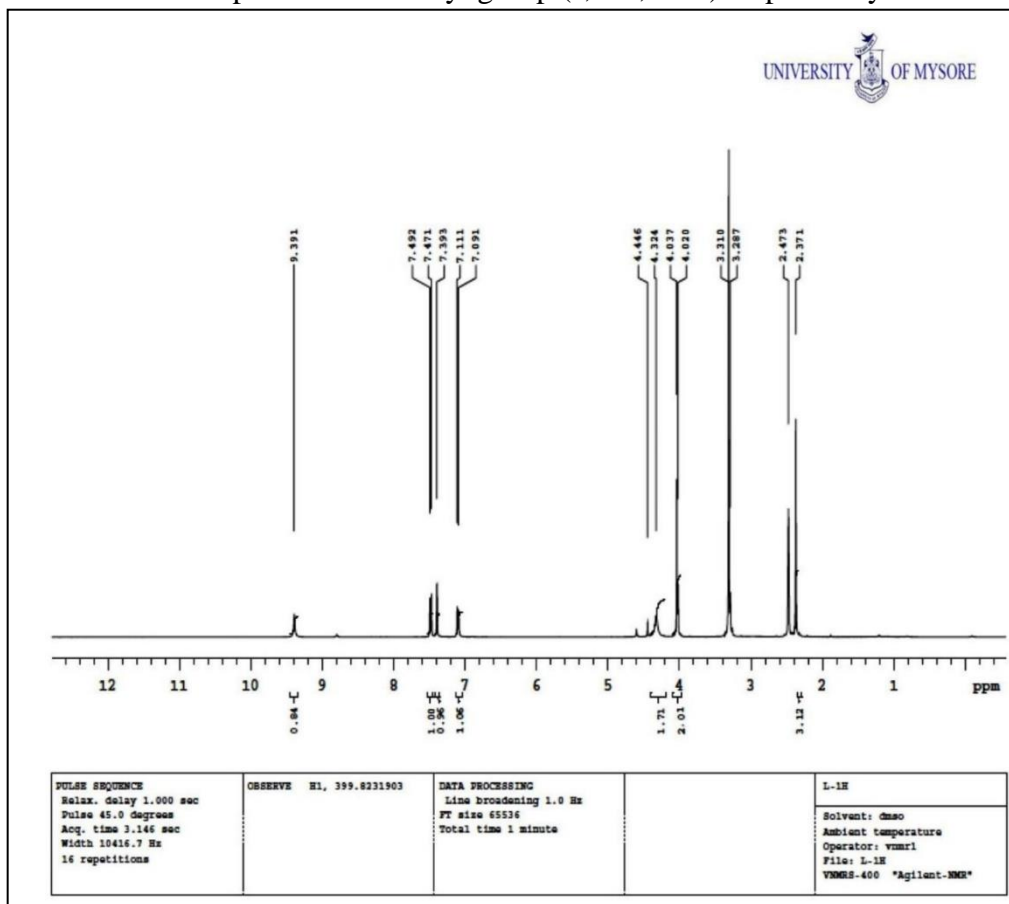

Figure 3. ^1H NMR spectrum of Ligand (MBA).

The ^{13}C NMR spectrum of MBA specified ten carbon atoms in a different environment which ranged from 21.32 to 166.00 ppm, respectively. A single peak resonating at 166.00 ppm

was assigned to the carbonyl carbon of the ligand, and another peak produced at 164.01 ppm was designated to the (–N=C–) of the oxazole ring. Further, six aromatic carbon atoms emerged at 109.99 to 149.92 ppm, and the peak at 34.29 ppm was referred to (–S–CH$_2$–). Lastly, the peak formed at 21.32 ppm ratified the presence of methyl carbon atom of benzoxazole ring. Because of the above-stated spectral observations, it is apparent that both ^{1}H NMR and ^{13}C NMR are consistent with the ligand's proposed molecular structure. A spectrum of ^{1}H NMR and ^{13}C NMR can be found in Figures 3 and 4.
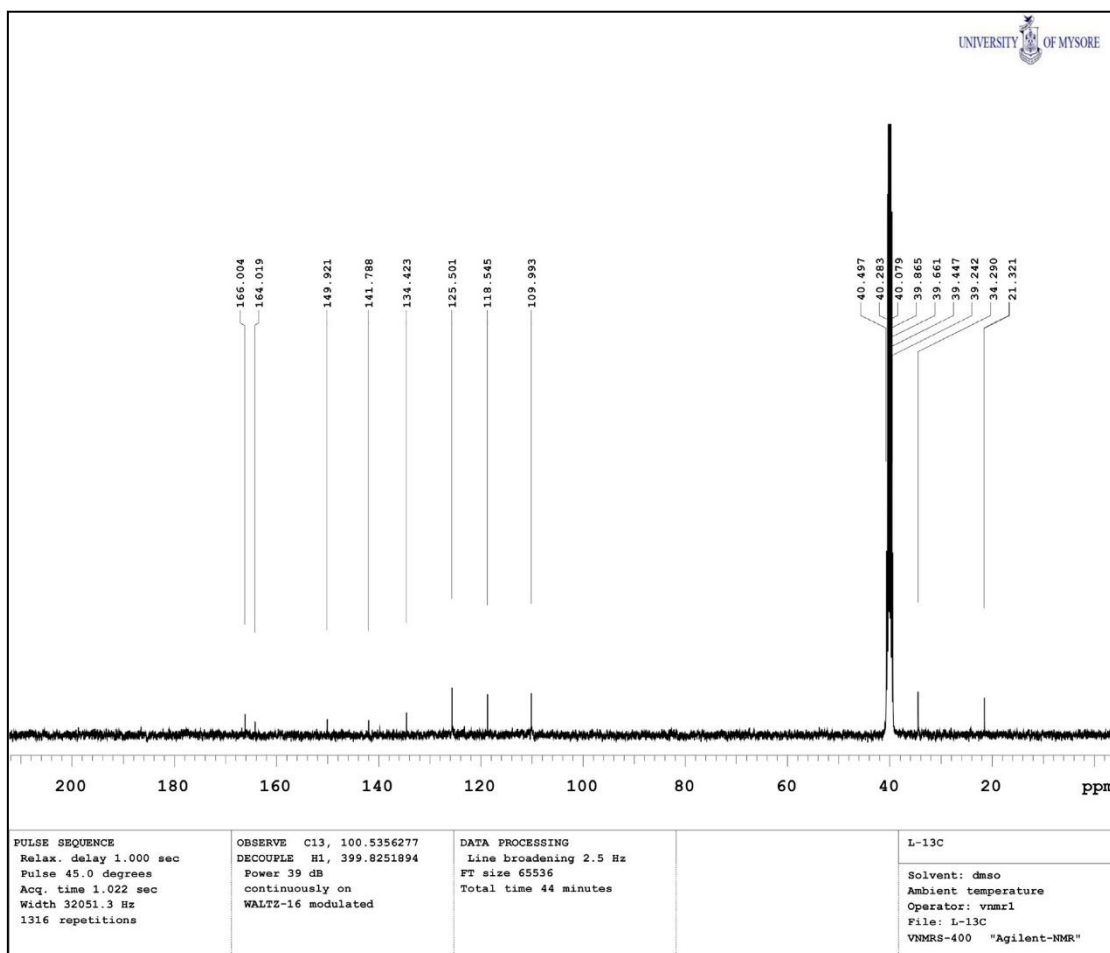

Figure 4. ^{13}C NMR spectrum of Ligand (MBA).

3.3. Mass spectral studies.

The molecular ion peak corresponded to their molecular weight alongside other fragment peaks in the mass spectrum of MBA and its coordinated compounds. The mass spectra of MBA displayed molecular ion peak [M+1] at m/z 238.06 (Cal: 237.27) (Figure 5a). Also, the mass spectra of metal complexes [Co(MBA)$_2$.Cl$_2$], [Ni(MBA)$_2$.Cl$_2$] and [Zn(MBA)$_2$.Cl$_2$] demonstrated molecular ion peaks [M+1] m/z at 605.02, 605.19 and 611.15 whereas mass spectra of [Cu(MBA)$_2$.Cl$_2$] showed molecular ion peak m/z at 609.38, respectively. The mass spectra of [Co(MBA)$_2$.Cl$_2$]and [Zn(MBA)$_2$.Cl$_2$] are represented in Figures 5b and 5c. It is possible from the above-interpreted data to infer that the peaks of molecular ions in both synthesized MBA and its metal complexes correlated with their molecular weight and thus affirms the 1:2 ratio between the metal and ligand.
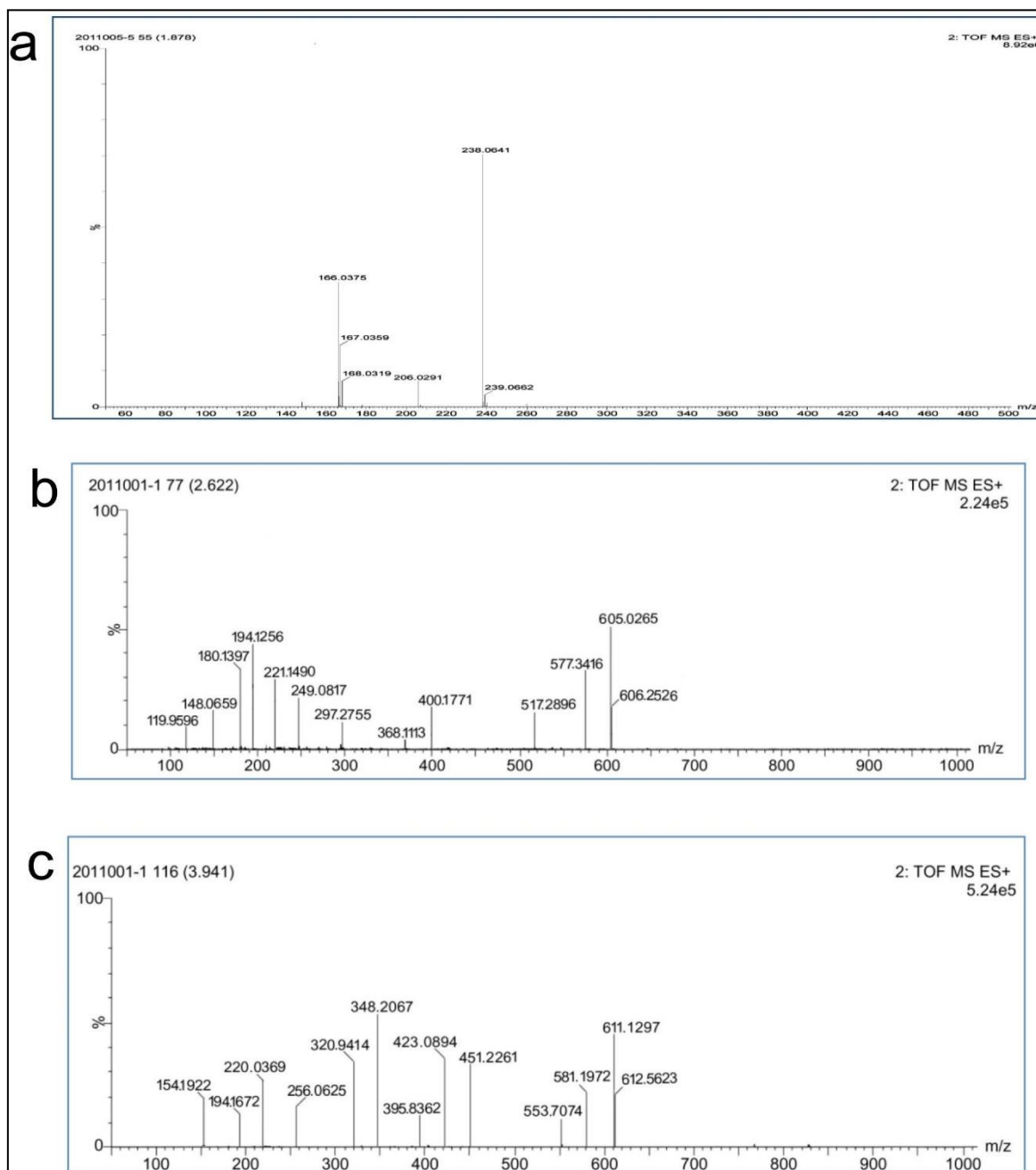
Figure 5. LC-MS spectrum of **(a)** Ligand (MBA); **(b)** Co(II) complex; **(c)** Zn(II)complex.

3.4. IR spectral studies.

IR spectrum of MBA and its d-block complexes were recorded in order to unravel the coordination mode between the ligand and its metal complexes. A list of the most notable IR absorption bands of MBA and its corresponding metal complexes is placed in Table 2, and the IR spectra of the latter compounds are presented in Figure 6(a-e). Taking into account the IR spectrum of MBA, double peaks were obtained at 3414 cm^{-1} because of v(-NH$_2$) stretching vibrations [21] as well as a sharp peak at 3302 cm^{-1} associated with v(-NH) stretching vibration, respectively. As for the IR spectrum of all the metal complexes, a larger difference was not observed in the peak position of either (-NH$_2$) or (-NH), proving their absence from the coordination process. Further, MBA and metal complexes displayed medium intensity aromatic (-CH) bands in the region of 3046-3051 cm^{-1}. Besides, MBA exhibited three intense sharp peaks at 1648 cm^{-1}, 1534 cm^{-1} and685 cm^{-1} due to v(C=O), v(C=N) and v(C-S) stretching vibrations. Whereas in the case of all the metal coordinated compounds, a shift was observed

towards the lower frequency side of both v(C=O) and v(C=N), ranging from 1576-1580 cm^{-1} and 1504-1511 cm^{-1}. This authenticated the role of the oxygen atom of the carbonyl group as well as the nitrogen atom of the benzoxazole ring in the complexation process with metal ions [22]. Additionally, the involvement of aforesaid groups in the structural formation of the complex was verified by the emergence of new peaks at 494-498 cm^{-1}, referred to as v(M-N) bonds, while the peaks at 571-576 cm^{-1} corresponded to v(M-O) bonds. Thus overall, IR data informs of the bidentate nature of ligand MBA bearing N,O donor sites.

Table 2. FTIR spectral data (cm^{-1}) of MBA and its metal complexes.

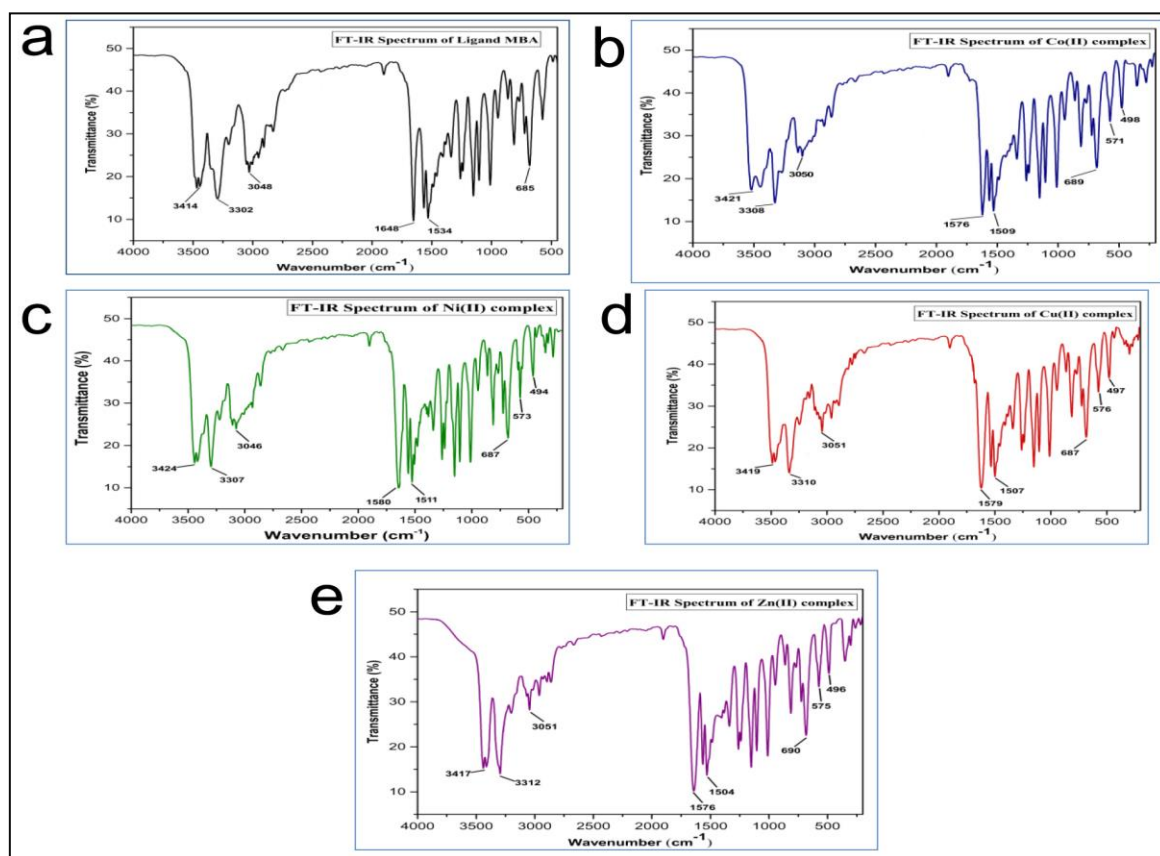| Compounds	v(-NH$_2$)	v(-NH)	v(Ar-CH)	v(C=O)	v (C=N)	v (C-S)	M-O	M-N
MBA	3414	3302	3048	1648	1534	685	---	---
[Co(MBA)$_2$.Cl$_2$]	3421	3308	3050	1576	1509	689	571	498
[Ni(MBA)$_2$.Cl$_2$]	3424	3307	3046	1580	1511	687	573	494
[Cu(MBA)$_2$.Cl$_2$]	3419	3310	3051	1579	1507	687	576	497
[Zn(MBA)$_2$.Cl$_2$]	3417	3312	3051	1576	1504	690	575	496

Figure 6. FT-IR spectra of **(a)** MBA ligand; **(b)** Co(II) complex; **(c)** Ni(II) complex; **(d)** Cu(II) complex;**(e)** Zn(II) complex.

3.5. Electronic spectra and magnetic moment studies.

The proposed geometries of each metallic complex were deduced by the electronic absorption spectra and magnetic susceptibility results shown in Table 3 and Figure 7—the light brown colored [Co(MBA)$_2$.Cl$_2$] exhibited two absorption bands at 613 and 681 nm indicating ^{4}T$_{1g}$(F) → 4A$_{2g}$ (F) (v_1) and ^{4}T$_{1g}$ (F) → ^{4}T$_{2g}$ (F) (v_2) transitions with magnetic moment value of 4.52B.M testifying an octahedral environment [23]—the wine red colored [Ni(MBA)$_2$.Cl$_2$] possessed two absorption bands at 429 and 515 nm denoted as ^{3}A$_{2g}$→^{3}T$_{1g}$ (P) and ^{3}A$_{2g}$→^{3}T$_{1g}$ (F) transitions acquiring a magnetic moment value of 2.88 B.M implying an octahedral

geometry [24], in case of dark brown colored [Cu(MBA)$_2$.Cl$_2$] two absorption shoulders at 472 nm were seen, which was assigned as charge transfer transition, while 574 nm attributed to $^2E_g \rightarrow {}^2T_{2g}$ transition and the magnetic moment value of 1.77 B.M was noticed. Hence an octahedral geometry was proclaimed[25].

Table 3. Electronic absorption spectral bands of metal complexes.

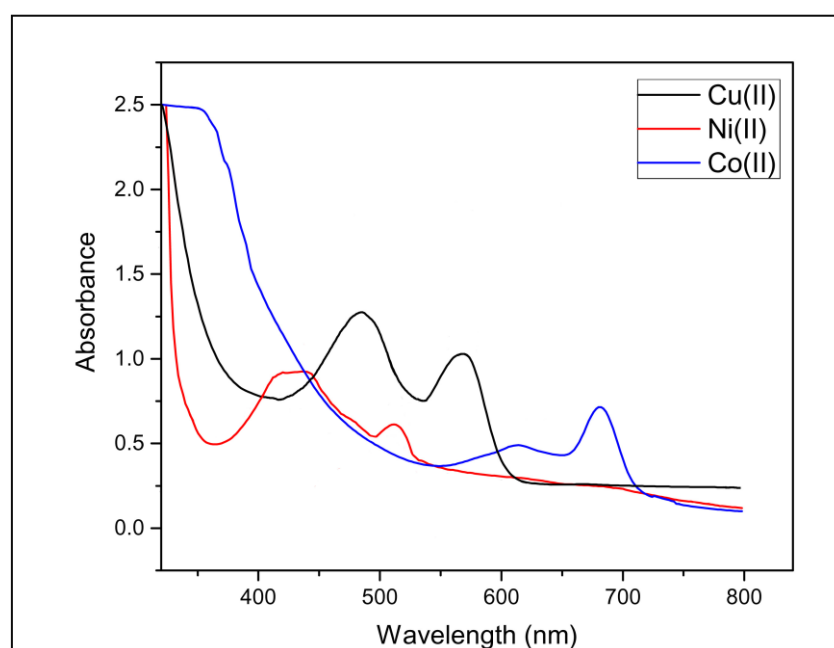| Compound	λ(nm)	Transitions	Magnetic moment (B.M)
[Co(MBA)$_2$.Cl$_2$]	613	$^4T_{1g}(F) \rightarrow 4A_{2g}(F)$ (ν$_1$)	4.52
	681	$^4T_{1g}(F) \rightarrow {}^4T_{2g}(F)$ (ν$_2$)	
[Ni(MBA)$_2$.Cl$_2$]	429	$^3A_{2g}(P) \rightarrow {}^3T_{1g}(P)$ (ν$_1$)	2.88
	515	$^3A_{2g}(F) \rightarrow {}^3T_{1g}(F)$ (ν$_2$)	
[Cu(MBA)$_2$.Cl$_2$]	472	$^2T_{2g} \rightarrow {}^2E_g$	1.77
	574		
[Zn(MBA)$_2$.Cl$_2$]	-	-	Dia

Figure 7. Electronic absorption spectral bands of MBA metal complex.

3.6. PX-ray studies.

The prepared metal complexes were partially soluble in common organic solvents, and thus single crystal study was not carried out. Henceforth to recognize the degree of crystalline nature of the metal complexes, the powder XRD diffraction of coordinated compounds of MBA was analyzed at 2θ=0-80º, where the notable sharp peaks were reported enumerating their crystalline nature. The details procured via the assessment of diffraction patterns of Co(II) and Zn(II) complexes are summed up in Tables 4 and 5, and the diffractograms are shown in Figures 8 (a) and (b). The Miller indices (hkl) with found and calculated interplanar space d, 2θ values were measured, and the orthorhombic crystal system was particularized for synthesized metal complexes. The average crystalline sizes of the complex were calculated by Debye Scherrer equation (D = K λ / β Cos θ), where D = Particle size, K; Dimensionless shape factor, λ=X-ray wavelength (0.15406 Å), β=Linebroadening at half the maximum intensity and θ=Diffraction angle. The Co(II), Ni(II), Cu(II), and Zn(II) complexes have a crystalline size of 19.60 nm, 7.56 nm, 8.80 nm, and 21.39 nm proving the nanocrystalline state of metal complexes.

Table 4. Powder XRD spectral data of Co(II) complex.

Peak No	2θ	θ (degree)	θ (radian)	Sinθ	hkl	d		a in Å
						Cal	Obs	
1	8.4673	4.2336	0.073	0.0737	110	10.434	10.112	3.62
2	10.8113	5.4056	0.094	0.0941	111	8.176	8.100	3.62
3	12.9585	6.4792	0.113	0.1127	200	6.826	6.223	3.62
4	14.7457	7.3728	0.128	0.1282	211	6.002	5.997	3.62
5	15.5185	7.7592	0.135	0.1349	211	5.705	5.321	3.62
6	17.6672	8.8336	0.154	0.1534	220	5.016	4.996	3.62
7	22.9315	11.4657	0.200	0.1986	321	3.875	3.221	3.62
8	28.7848	14.3924	0.251	0.2484	332	3.099	3.012	3.62

Table 5. Powder XRD spectral data of Zn(II) complex.

| Peak No	2θ	θ (degree)	θ (radian)	Sinθ	hkl	d		a in Å
						Cal	Obs	
1	11.3522	5.6761	0.099	0.0988	111	7.788	7.443	10.24
2	16.3383	8.1691	0.142	0.1420	211	5.420	5.321	10.24
3	18.3737	9.1868	0.160	0.1595	220	4.824	4.112	10.24
4	18.9542	9.4771	0.165	0.1645	220	4.678	4.270	10.24
5	19.6682	9.8341	0.171	0.1707	221	4.510	4.221	10.24
6	21.161	10.5805	0.184	0.1835	310	4.195	4.065	10.24
7	22.4496	11.2248	0.195	0.1945	222	3.957	3.221	10.24
8	24.0217	12.0108	0.209	0.2079	320	3.701	3.335	10.24
9	24.7202	12.3601	0.215	0.2139	321	3.598	3.287	10.24
10	26.9007	13.4503	0.234	0.2324	400	3.311	3.231	10.24
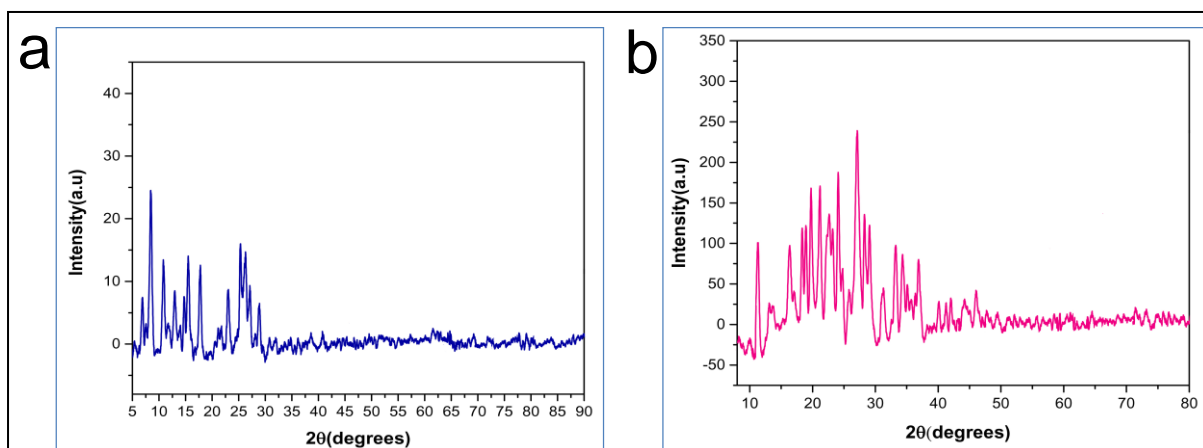
Figure 8. P-XRD pattern of **(a)** Co(II) complex; **(b)** Zn(II) complex.

3.7. Thermal analysis.

Thermogravimetric measurements were carried out to examine the thermal decomposition of Co(II), Ni(II), Cu(II), and Zn(II) complexes. Table 6 and Figure 9(a-d) describe the thermal stability data in detail. The thermoanalytical curve of both Co(II) and Cu(II) complex was achieved in three steps where Co(II) complex had initial degradation bearing the mass loss of 11.29%(cal:11.73%) and DTG peak at 141°C signaling the ejection of two chloride ions in the temperature 127-154°C. The second TG curve acquired between 286-320 °C had a mass loss of 43.86% (cal:44.00%), indicating evidence for the elimination of two benzoxazole molecules with a DTG peak at 304 °C. In the third TG curve, a mass depletion of 31.75% (cal:31.90%) was recorded between 405-457°C stating the eviction of organic moiety ($C_4H_{16}N_4OS_2$) with the DTG peak occurring at 424°C, leaving the stable CoO residue 12.32% (cal:12.40%) in the temperature range 662-694°C.

Likewise, the Cu(II) complex displayed its first breakdown, bearing a mass deterioration of 11.52% (cal:11.64%) with a DTG peak at 141°C, hinting at the expulsion of

two chloride ions at a temperature range of 127-157°C. The second TG curve was noted at the temperature of 189-222°Cwith a reduced mass of 43.00% (cal:43.72%), referring to the ejection of two benzoxazole molecules with a DTG peak at 200°C. The third TG curve was procured at the temperature of 257-301°C with a mass loss of 31.32% (cal:31.47%) and a DTG peak at 276°C, implying the disappearance of organic moiety ($C_4H_{16}N_4OS_2$) and the stable CuO residue 12.98% was leftover(cal:13.06%) in the temperature range 609-664°C.

Table 6. Decomposition steps and weight loss of metal complexes.

| Compounds	Decomposition steps	Temperature range (°C)	DTG$_{max}$ (°C)	Removed species	Wt.loss(%) found(calculated)
[Co(MBA)$_2$.Cl$_2$]	I	127-154	141	-(Cl$_2$)	11.29% (11.73%)
	II	286–320	304	-(C$_{16}$H$_{14}$N$_2$O$_2$)	43.86% (44.00%)
	III	405-457	424	-(C$_4$H$_{16}$N$_4$OS$_2$)	31.75% (31.90%)
	Residue	662-694		CoO	12.32% (12.40%)
[Cu(MBA)$_2$.Cl$_2$]	I	127-157	141	-(Cl$_2$)	11.52% (11.64%)
	II	189-222	200	-(C$_{16}$H$_{14}$N$_2$O$_2$)	43.00% (43.72%)
	III	257-301	276	-(C$_4$H$_{16}$N$_4$OS$_2$)	31.32% (31.47%)
	Residue	609-664		CuO	12.98% (13.06%)
[Ni(MBA)$_2$.Cl$_2$]	I	267-335	294	(C$_{16}$H$_{14}$N$_2$O$_2$S$_2$Cl$_2$)	65.98% (66.02%)
	II	471-561	513	-(C$_4$H$_{16}$N$_4$O)	21.11% (21.23%)
	Residue	682-756		NiO	12.20% (12.36%)
[Zn(MBA)$_2$.Cl$_2$]	I	273-310	276	(C$_{16}$H$_{14}$N$_2$O$_2$S$_2$Cl$_2$)	64.29% (65.15%)
	II	460-550	494	-(C$_4$H$_{16}$N$_4$O)	21.09% (21.14%)
	Residue	726-765		ZnO	13.03% (13.34%)
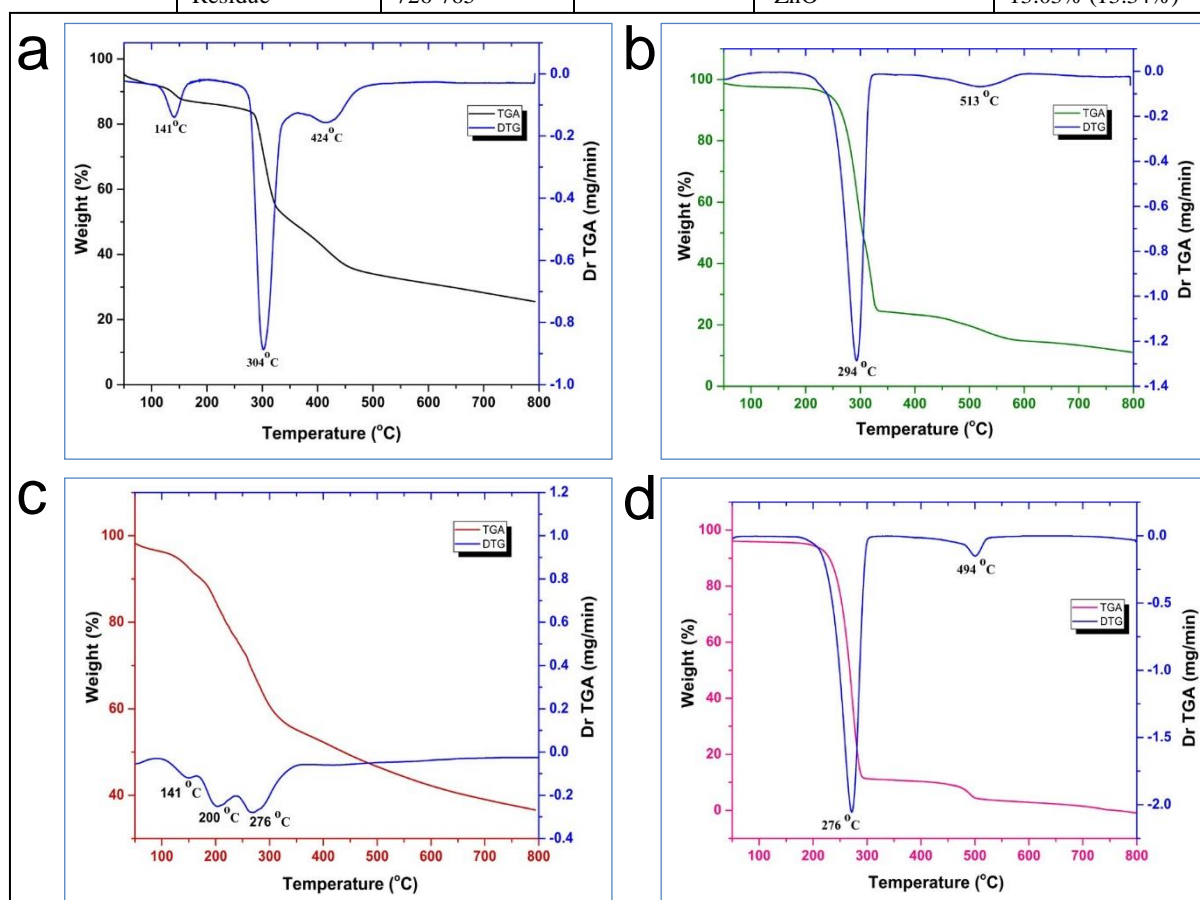
Figure 9. TGA and Dr-TGA curves of **(a)** Co(II) complex **(b)** Ni(II) complex**(c)** Cu(II) complex **(d)** Zn(II) complex.

Incase of Ni(II) and Zn(II) complexes, a two-stage depletion pattern was seen where the thermoanalytical curve of Ni(II) complex demonstrated that the initial step of

decomposition was followed by a reduced mass of 65.98% (cal:66.02%), with the DTG peak at 294 °C remarking the eviction of an organic moiety with two chlorine ions ($C_{16}H_{14}N_2O_2S_2Cl_2$) in the temperature 267-335ºC. The second degradation was achieved with a mass reduction of 21.11%(cal:21.23%), pointing to the elimination of organic moiety ($C_4H_{16}N_4O$) in the temperature of 471-561ºC with a DTG peak at 513 °C and the stable NiO residue was left behind 12.20% (cal:12.36%)in the temperature 682-756 ºC. Similarly, Zn(II) complex showcased its first TG curve with a mass decrement of 64.29% (cal:65.15%), having a DTG peak at 276 °C, revealing the elution of organic moiety with two chloride ions ($C_{16}H_{14}N_2O_2S_2Cl_2$) in the temperature 273-310 ºC. The second step of decomposition took place bearing a reduced mass of 21.09% (cal:21.14%) with DTG peak-peak at 494 °C, denoting the removal of organic moiety ($C_4H_{16}N_4O$) between the temperature 460-550ºC leaving behind the stable residual ZnO 13.03% (cal:13.34%) in the temperature of 726-765ºC.

3.8. Kinetic studies.

In order to study thermal systems kinetically, various equations have been applied. A large number of these equations comprise a relation between mass and temperature, which elucidates various aspects of the degradation process. In the present study, kinetic parameters examination from TGA curves was performed by adopting Broido's method. Plots of ln(ln 1/y)versus 1000/T (where y is the fraction not yet decomposed) for different stages of the thermal degradation of the complexes are shown in Supplementary Information (Figure S1), and the data are tabulated in Table 7.

The slope of the plot ln(ln 1/y) versus 1000/T is related to the energy of activation as,

$$E_a = -2.303 \times R \times slope$$

where, R = gas constant.

The parameters, enthalpy (ΔH^*), entropy (ΔS^*), and Gibbs free energy (ΔG^*) of activation were calculated using the following typical equations,

$$\Delta H^* = E_a - R\, T_d$$
$$\Delta S^* = \Delta H^*/T - 4.576 \log T/K' - 47.22 \text{ where } K' = -\ln(\ln 1/y)$$
$$\Delta G^* = \Delta H^* - T\Delta S^*$$

Using the collected results, it was understood that the activation energies of decomposition were in the range (0.93-8.12), (0.75-5.34), (10.55-11.06), and (19.62-54.51) kJ mol^{-1} for Co(II), Cu(II), Ni(II) and Zn(II) complexes respectively. In addition to testifying to the thermal stability of complexes, positive 'E$_a$' values also showed that decomposition reactions progressed at a normal pace.

Table 7. Thermodynamic data of the thermal decomposition of metal complexes.

Compounds	Stage	Ea (kJ/mol)	lnA min^{-1}	ΔH^* (kJ/mol)	ΔS^* (kJ/mol)	ΔG^* (kJ/mol)
[Co(MBA)$_2$.Cl$_2$]	1st	0.936	3.579	0.227	-131.377	18.164
	2nd	9.944	6.057	7.374	-152.747	54.598
	3rd	8.122	4.923	4.575	-149.374	68.314
[Cu(MBA)$_2$.Cl$_2$]	1st	0.750	1.955	0.415	-159.900	22.826
	2nd	2.654	3.281	0.975	-156.727	31.845
	3rd	5.345	4.368	2.984	-153.574	46.581
[Ni(MBA)$_2$.Cl$_2$]	1st	10.551	6.461	8.106	-153.106	53.128
	2nd	11.067	5.495	6.223	-146.262	81.579
[Zn(MBA)$_2$.Cl$_2$]	1st	19.620	10.612	17.336	-153.851	59.596
	2nd	54.516	16.685	50.400	-141.912	120.657

Besides, for the metal(II) complexes, the positive values of 'ΔG^*' support the notion that the final residue has greater free energy than the initial compound and that all

decomposition steps are non-spontaneous. Further, the positive values of 'ΔH*'implied endothermic decomposition, and at last negative values of 'ΔS*'recommended an orderly structure of the activated complexes as compared to those of the reactants [26-27].

3.9. Scanning Electron Microscopy (SEM).

The surface morphology of MBA and its metallic complexes was identified with scanning electron microscopy (SEM), and the SEM images of analyzed compounds are picturized in Figure 10. A tiny spherical-shaped dispersed structure was observed for the ligand MBA, whereas a bundle of needle-shaped morphology was exhibited by Co(II) complex. The Ni(II) complex displayed crystalline rice grain-like structure, and both Cu(II) and Zn(II) complex showcased rod-shaped morphology, respectively.
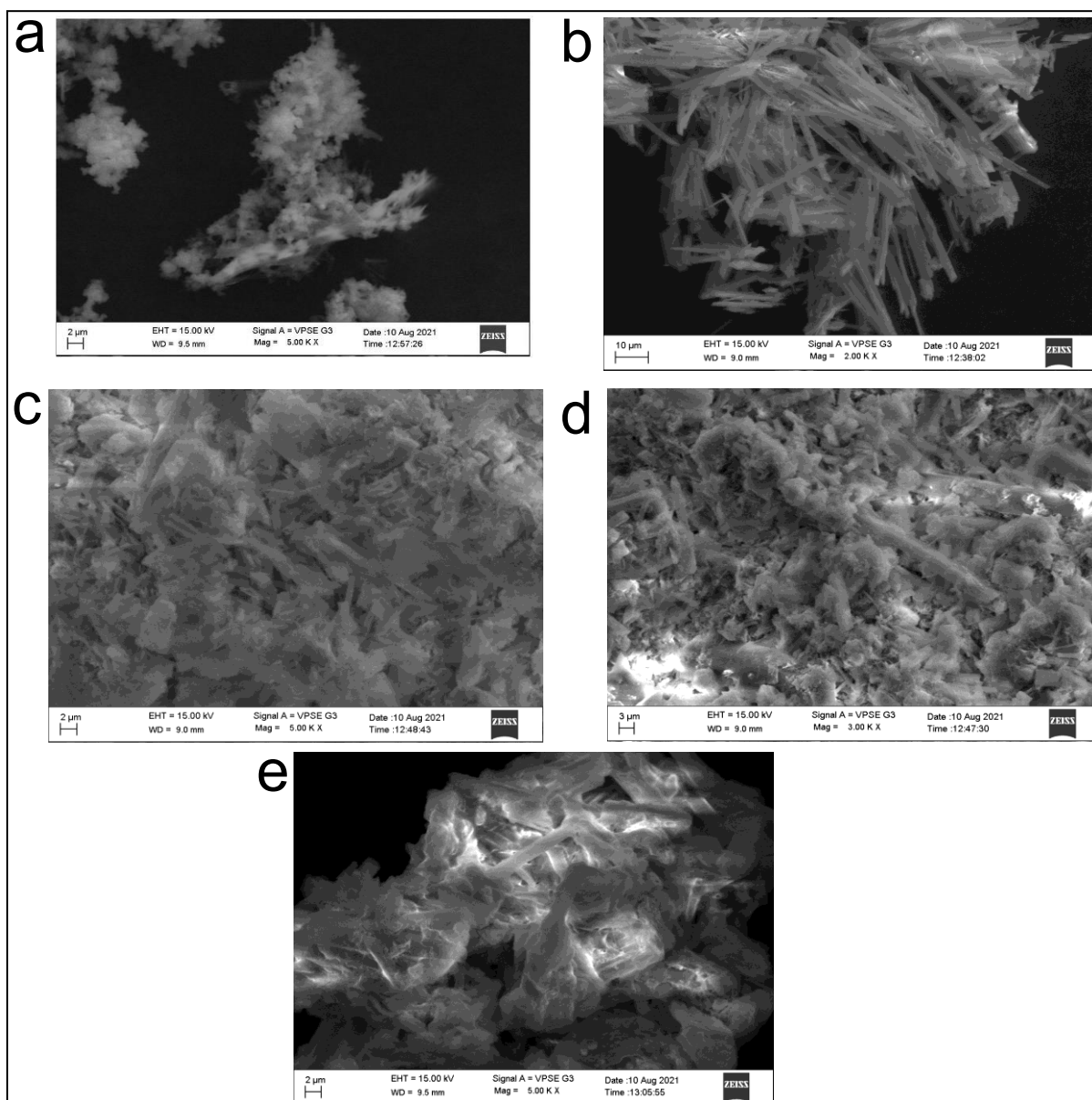

Figure 10. SEM morphology **(a)** Ligand (MBA);**(b)** Co(II) complex;**(c)** Ni(II) complex;**(d)** Cu(II) complex;**(e)** Zn(II) complex.

3.10. Electrochemical studies.

3.10.1. characterization of different modified electrodes.

Different electrodes were electrochemically studied via CV techniques in the absence and presence of H_2O_2 at -0.1 to 1.0 V v/s Ag/AgCl at the scan rate of 50 mVs^{-1}. It was noted that Co(II) MBA/GCE with a thin film layer enhanced the peak current by narrowly shifting it to a negative peak potential in contrast to the bare electrode and modified electrode. Further, under N_2 atmosphere alongside H_2O_2, cyclic voltammogram analysis of Co(II)MBA/GCE was carried off in pH-7 buffer solution where the modified electrode signal was located at the potential of -0.4V. A comparison of the bare electrode to the Co(II)MBA/GCE strongly proclaimed that the modified electrode was electrocatalytic active, and it accurately detected the $H_2O_{2,}$as highlighted in Figure 11.
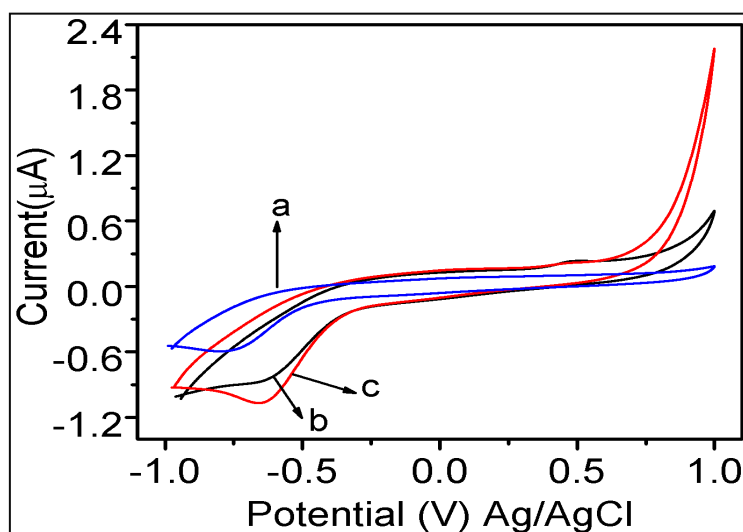

Figure 11. Cyclic voltammograms of **(a)** bare GC;**(b)** modified GCE in the absence of H_2O_2; **(c)** modified GCE in the presence of H_2O_2 in pH-7 buffer solution at the scan rate of 50 mVs-1.

3.10.2. Electrocatalysis evaluation of H_2O_2 reduction.

Figure 12(a) presents cyclic voltammograms for Co(II)MBA/GCE with various concentrations of H_2O_2. The electrochemical inspection was performed for modified electrodes as well as electrocatalytic reduction of H_2O_2 in PBS (pH-7). The catalytic reduction of H_2O_2 is facilitated by the oxidizing peak of the metal complex at −0.69 V. An inset linear plot of H_2O_2 concentration v/s reduction peak current is represented in Figure 12(b). There was an upsurge in reduction peak current with a decrease in the overpotential for the reduction of H_2O_2 on Co(II)MBA/GCE compared to bare GCE. This tremendous upsurge in reduction peak current was seen for Co(II)MBA/GCE compared to bare GCE, and an elevation in peak current with the increase in the concentration of H_2O_2 was also witnessed. The linear response in the catalytic reduction current was recorded during H_2O_2 detection in the concentration range of 0.5 to 06 μM for Co(II)MBA/GCE at −0.69 V. Inset Figure 12(b) also illustrates the linear relationship between the reduction current and the varied concentration of H_2O_2. Because of the exceptional physicochemical activity of the prepared cobalt complex, the linear concentration range and respective reduction currents gained forCo(II)MBA/GCE seemed to be higher than the bare GCE. The linear response noticed for reduction peak current v/s concentration of H_2O_2 satisfied the straight line equation that is, y = - 4.150 (H_2O_2)- 8.2955

with the sensitivity ($\Delta y/\Delta x$) 4.150 µAµM^{-1} and LOD 0.166 µmolL^{-1} and LOQ 0.48µmolL^{-1}for Co(II)MBA/GCE, respectively.
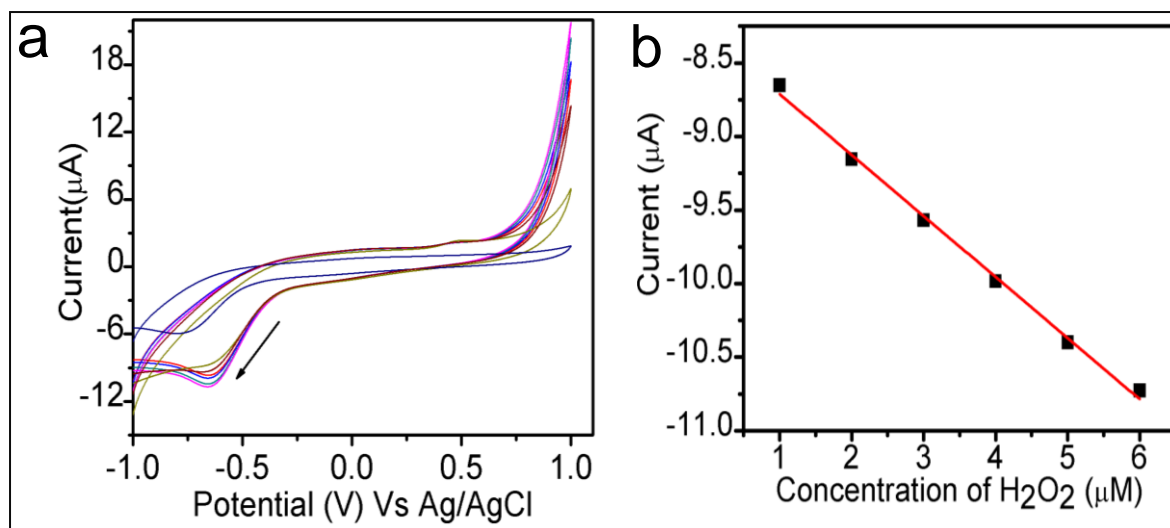

Figure 12. Cyclic voltammograms of **(a)** Co(II)MBA/GCE at different concentration of H$_2$O$_2$ (0.5 -10 µM)in PBS (pH-7) at scan rate of 50 mVs^{-1}; **(b)** Inset calibration current v/s concentration of H$_2$O$_2$.

3.10.3. Effect of Scan rate of H$_2$O$_2$.

Peak current responses were intensified with increased scan rates. As shown in Figure13(a), the current intensity elevated linearly with increasing scan rate (10-100 mVs^{-1}). The linear relationship between the reduction peak currents and the square root of scan rate ($v^{1/2}$) in response to H$_2$O$_2$ was explored and is showcased in Figure 13(b). Analytical data of the modified electrode for the detection of H$_2$O$_2$ corresponding to the effect of scan rate was recognized. The obtained sensitivity of 4.643 µAµM^{-1} and linear regression equation Ip (µA) = 4.6432x - 1.353 and R^2 = 0.983 manifested that the Co(II)MBA/GCE was indulged in diffusion-controlled mass transfer activities. We have compared the various CV parameters of Co(II)MBA/GCE with that of previously described modified electrodes for the determination of H$_2$O$_2$ in Table 8.
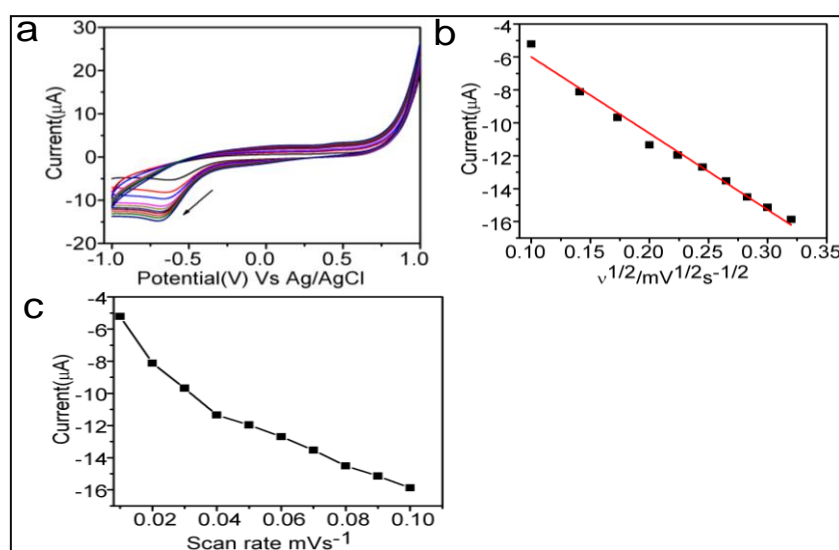

Figure 13. (a) Cyclic voltammogram of Co(II)MBA/GCE recorded in PBS (pH =7) at different scan rates: 10 to 100 mVs^{-1}; **(b)** Inset calibration curves of the square root of scan ratev/s peak current; **(c)** scan rate v/s peak current.

3.10.4. Electrochemical sensing of glucose using the chemisorbed Co(II) complex modified electrode.

Figure 14(a) denotes the electrocatalytic performance of the Co(II)MBA/GCE, which detects the peak potential (440 mV) in PBS (pH-7) solution containing different glucose concentrations ranging from 0.5 to 10 μM. It was also noticed that positive peak potential (530 mV)optimizes positive current as glucose concentration increases. From this, it can be inferred that Co(II)MBA/GCE demonstrated impressive catalytic capability toward the electro-oxidation of varying glucose concentrations. The variation of the peak current at 440 mV v/s glucose concentration and linear concentration range was found to be 0.5 to 10 μM with a high sensitivity, linear regression equation and correlation coefficient of 0.0247 μAμM^{-1} cm^{-2} y = 0.02447x + 0.5894 andR^2 = 0.999 as shown in Figure 14(b). These results pointed out that Co(II)MBA/GCE has worthy operational stability, linear responses, LOD 0.16 μmol L^{-1}, and LOQ 0.5 μmol L^{-1}. A comparison of the cobalt-modified electrode with priorly reported modified electrodes for the detection of glucose is discussed in Table 8.
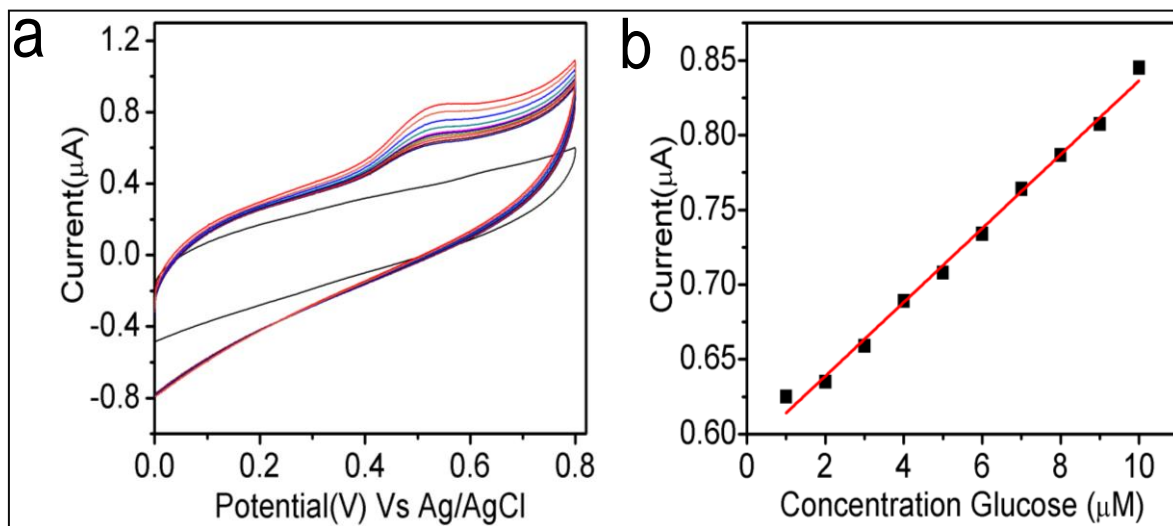

Figure 14. Steady-state cyclic voltammograms of **(a)** in a solution containing different concentration of glucose 0.5-10 μM in PBS sweep rate of 50mVs^{-1}; **(b)** Inset calibration curve of concentration v/speak current.

3.10.5. Effect of Scan rate of glucose.

In Figure 15, the resulting electrochemical plots from glucose analysis can be observed. Upon maximizing the scan rate (10-200 mV/s) of Co(II)MBA/GCE in PBS (pH=7), the peak potential was detected at 515 mV. Observations confirmed that the oxidation peak currents escalated with an increase in the square root of the scan rate. Figure 15(a) emphasized that Co(II)MBA/GCE current was proportional to the square root of scan rate, the linear regression equation being Ip(μA)= 0.0247 x [v]$^{1/2}$(mV/s)$^{1/2}$ + 0.5895 and the plots proved excellent linearity with correlation coefficients of R^2 = 0.9936. The results also showed that Co(II)MBA/GCE goes through an adsorption process.
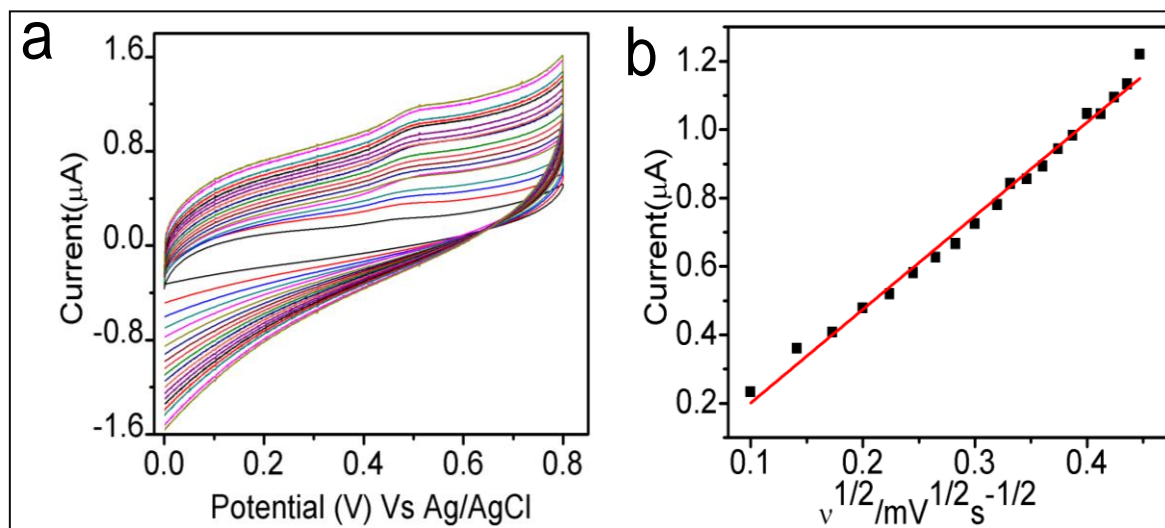
Figure 15. CV of **(a)** Co(II)MBA/GCE in 0.5 µL of glucose at different sweep rates from to 200 mVs^{-1}; **(b)** plots of Ip v/s $v^{1/2}$/mV$^{1/2}$s$^{-1/2}$.

3.10.6. Simultaneous detection of H_2O_2 and glucose using Co(II)MBA/GCE.

The cyclic voltammetric curve was recorded for simultaneous determination of glucose and H_2O_2 in buffer solution using Co(II)MBA/GCE electrode at a scan rate of 50 mVs^{-1}, as shown in Figure 16. The voltammograms of the binary mixture comprising glucose and H_2O_2 were very much separated and exhibited two clearly defined and distinguishable anodic and cathodic peak currents. The peak potential is relative to the oxidation and reduction of glucose and H_2O_2, which coordinated well with their individual anodic and cathodic peak potentials, are depicted in Figure 16. On adding 03 µmolL−1 of glucose, an increment in positive peak current 4.252 µA was noticed at a positive peak potential of 0.515 V, which was consistent with the potential observed during individual detection of glucose. Likewise, adding H_2O_2 resulted in an increase in negative peak current of -16.23 µA with a negative peak potential of -0.69 V. This recorded peak potential was also equivalent to the potential gained during the individual analysis of hydrogen peroxide.

The bare electrode was initially preferred for simultaneous glucose and H_2O_2 analysis, but it failed to display any peak currents in the given range (Figure 16(a)). Later addition of 03 µmolL^{-1} glucose led to the minor growth of peak current (Figure 16(b)). Finally, in the presence of both glucose and H_2O_2 at concentrations 03 µmolL^{-1} and 05 µmol L^{-1}, a large enhancement in peak current was observed at 4.25×10^{-6} and -16.2319×10^{-6} and the same peak potential ~0.515 and -0.69 V was achieved compared to individual investigation of both the analytes (Figure 16(c)). Hence, it is apparent that applying the Co(II) MBA/GCE electrode is effective for the simultaneous CV determination of glucose and H_2O_2.

Table 8. Comparison of various modified electrodes for the detection of Glucose and H_2O_2.

Electrodes	Detection methods	Samples	Linear range (µmol/L)	Sensitivity (µAµM^{-1})	LOD (µmol/L)	Reference
GOx/Pt-PPy/Anodisc	CV	Glucose	1.75-3.2	67.19	0.89	28
GOx/CS/Au-GR/Au	CV	Glucose	2-10	17	180	29
Nafion/GOx/Pd-HCNFs/GCE	CV	Glucose	0.06-6	13	30	30
PPy on Pt/alumina electrode	CV	Glucose	0.5-10.4	7.4	30	31
Co$_3$O$_4$ UNS-Ni(OH)$_2$/GCE	CV	Glucose	5-40	1.089	1.08	32
GOx -GQDs	CV	Glucose	3-10	0.00769	1.35	33
Co(II)MBA/GCE	CV	Glucose	0.5-10	0.0247	0.160	This work

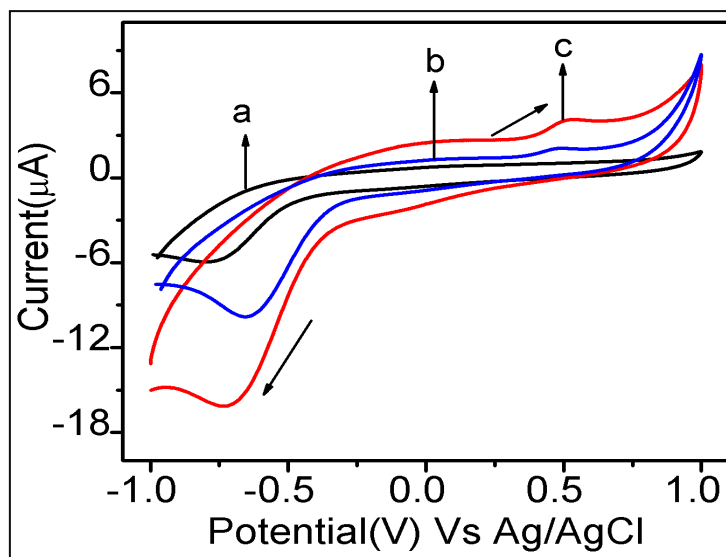| Electrodes	Detection methods	Samples	Linear range ($\mu mol/L$)	Sensitivity ($\mu A \mu M^{-1}$)	LOD ($\mu mol/L$)	Reference
GO/MnO$_2$	CV	H$_2$O$_2$	5-600	38.2	0.8	34
Co$_3$O$_4$/MWCNTs/gelatin/HRP	CV	H$_2$O$_2$	0.74-19	-	0.74	35
Cs-Cu-sal/C electrode	CV	H$_2$O$_2$	-	0.35	0.9	36
GC/APS(SG)–Ag NP	CV	H$_2$O$_2$	-	0.042	25	37
CeO$_2$-fructose	CV	H$_2$O$_2$	1-10	9.6	2.0	38
Co(II)MBA/GCE	CV	H$_2$O$_2$	0.5-6	4.150	0.166	This work

Figure 16. CV of (**a**) bare electrode with; (**b**) Co(II)MBA/GCE at a concentration of 03 $\mu molL^{-1}$ with glucose; (**c**) glucose (03 $\mu mol\ L^{-1}$), H$_2$O$_2$ (05 $\mu mol\ L^{-1}$) on Co(II)MBA/GCE at 50 mVs^{-1} in PBS.

Reproducibility and repeatability occupy a profound place in the designing of sensors. To verify the reproducibility of Co(II)MBA/GCE, 10 thin film-coated electrodes were fabricated for each modified film. With the aid of CV, H$_2$O$_2$ was detected for all of the fabricated modified electrodes by utilizing 05 μM H$_2$O$_2$ solutions. Co(II)MBA/GCE, on the other hand, had a general standard deviation of 3.6 % for each electrode. In four duplicates, the CV was conducted to detect the same H$_2$O$_2$ concentrations utilizing Co(II) MBA/GCE in PBS to study the repeatability of electrode measurements. Accordingly, the RSD for Co(II) MBA/GCE was observed to be 3.4%, and these values were within the acceptable limits, thus working adequately as a repeatable and reproducible electrochemical sensor. The modified electrode was scrutinized for its stability by comparing the CV response of the newly prepared electrode to the response of the electrode stored for a week. Interestingly, the CV current response of an electrode stored for a week was very close to its initial response indicating electrode stability over time. At the point where the electrodes were scanned for 25 and 50 cycles, only a peak current loss of 4% was documented for the electrodes, which ensured the outstanding electrochemical stability of Co(II)MBA/GCE.

3.11. Bioactivity studies.

3.11.1. Antimicrobial activity.

The antimicrobial activities of MBA and its metal complexes were tested *in vitro* against variant bacteria and fungi strains. Values have been grouped in Table 9 and graphed in Figures 17(a) and (b). Overall, the antimicrobial screening evidenced that the metal complexes were more productive under similar experimental conditions than the MBA ligand, with

inhibitory zones ranging from 11 to 26 mm. Furthermore, the intensified activity in metal complexes can be clarified by Overtone's theory and Tweedy's Chelation hypothesis [39]. As per Overtone's concept of cell permeability, liposolubility serves as the key criterion for monitoring antibacterial and antifungal activity. Coordination notably lessens the polarity of the metal ion since its positive charge is not sufficiently shared with the donor group and optimizes the delocalization of p and d electrons through the chelate ring. As a result of chelation, the centrally placed metal ions are more lipophilic, which further optimizes their penetration through the lipid layer of the cell membrane. In addition to interfering with the process of cellular respiration, these complexes impede the synthesis of proteins which hampers the growth of an organism and, consequently, leads to the death of microorganisms. Besides chelation, the nature of the metal ion and ligand, coordinating sites, the geometry, concentration, and hydrophilicity of the complexes also have an impact on microbial activity. Compared to MBA and the rest of the metal complexes, Ni(II) and Cu(II)complexes are proclaimed to be more toxic and effective towards the microbes and fungi with eminent zones of inhibition values.

**Table 9.** Antimicrobial activity of MBA & its metal complexes inhibition zone in mm.

Compound	Antibacterial activity								Antifungal activity			
	E.coli		*S.typhi*		*S.aureus*		*B.subtilis*		*A.niger*		*C. albicans*	
	100	200	100	200	100	200	100	200	100	200	100	200
MBA	12±0.47	18±1.15	11±0.57	16±0.47	11±0.47	13±0.57	10±1.15	13±1.52	10±0.57	13±1.15	10±0.57	12±0.47
[Co(MBA)₂.Cl₂]	14±1.52	21±1.15	12±1.15	22±1.52	15±0.57	20±1.15	13±1.52	19±0.57	13±0.47	21±1.52	13±1.15	18±1.52
[Ni(MBA)₂.Cl₂]	19±1.52	25±1.15	18±0.47	21±0.57	18±1.15	26±0.47	19±1.15	22±1.15	17±1.15	23±1.52	15±1.15	18±1.15
[Cu(MBA)₂.Cl₂]	18±0.57	23±0.47	17±1.15	23±1.52	19±1.15	21±1.52	17±0.47	20±1.52	16±0.47	22±0.57	14±0.47	16±1.52
[Zn(MBA)₂.Cl₂]	13±0.57	19±0.47	12±0.57	16±0.47	11±1.52	15±0.57	12±1.15	18±0.47	11±1.15	15±0.47	11±0.57	16±1.15
Std 1	26±0.47	29±0.57	28±0.57	30±0.47	26±0.57	32±0.47	26±1.15	30±1.52	-	-	-	-
Std 2	-	-	-	-	-	-	-	-	25±0.57	28±0.47	22±1.15	26±1.52

*Std 1: Chloramphenicol, Std 2: Fluconazole.
*Each value is expressed as the mean ± SD of three replicates for the zone of inhibition.
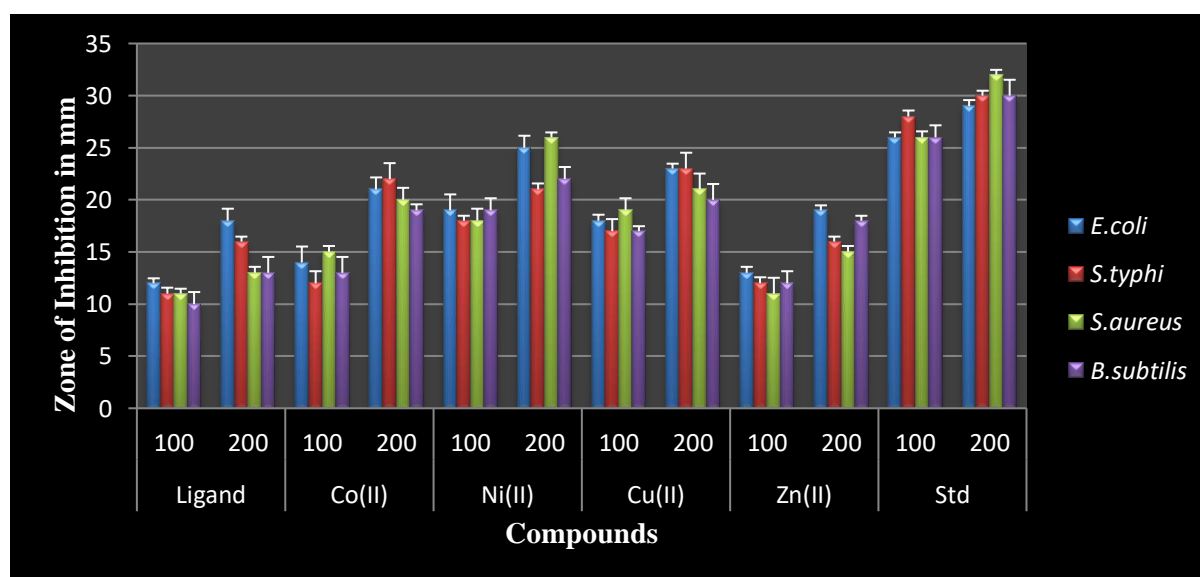
(a)
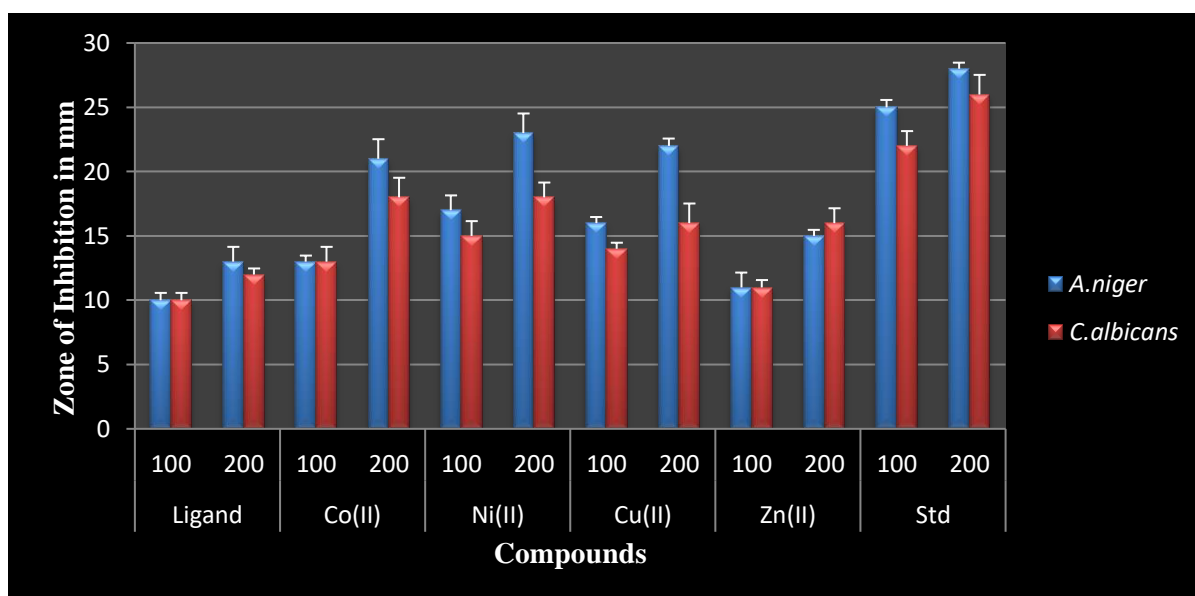
(**b**)

Figure 17. (a) Antibacterial activity ligand MBA and its metal complexes.**(b)** Antifungal activity of ligand MBA and its metal complexes.

As another aspect of this study, the MIC values for MBA and its metal coordinated compounds were determined using strains of bacteria and fungi, justifying that Ni(II) and Cu(II) complexes' own potential results relative to the free ligand and other metal complexes. Tables 10 and 11 contain the comparative data of MIC. Following the overall data of the biological activity of MBA as well as its metal complexes, it is proven that the biological activity follows the pattern:Ni(II)>Cu(II)>Co(II)>Zn(II)>Ligand.

Table 10. MIC data of antibacterial activity of MBA & its metal complexes inhibition zone in mm.

Compound	Antibacterial activity							
	E.coli				S.aureus			
	100	50	25	12.5	100	50	25	12.5
MBA	26±0.47	28±0.47	25±0.47	27±0.57	26±0.47	28±0.57	28±1.15	29±1.52
[Co(MBA)$_2$.Cl$_2$]	16±0.47	17±1.52	18±0.47	18±0.47	19±0.57	19±0.47	18±0.57	17±1.15
[Ni(MBA)$_2$.Cl$_2$]	12±1.15	11±1.52	13±1.15	11±0.47	11±0.57	12±1.15	12±0.47	14±0.57
[Cu(MBA)$_2$.Cl$_2$]	15±1.15	13±0.57	15±0.47	14±0.57	15±0.47	13±1.15	12±0.47	12±0.57
[Zn(MBA)$_2$.Cl$_2$]	21±0.47	18±0.57	20±1.15	19±1.52	19±0.47	20±0.47	22±0.57	18±0.47
Std 1	10±0.57	08±0.47	09±0.47	07±0.57	09±1.52	10±0.47	10±1.15	08±0.47

*Std 1: Chloramphenicol.

*Each value is expressed as the mean ± SD of three replicates for the zone of inhibition.

Table 11 . MIC data of antifungal activity of MBA & its metal complexes inhibition zone in mm.

Compound	Antifungal activity							
	A.niger				C.albicans			
	100	50	25	12.5	100	50	25	12.5
MBA	30±0.47	30±0.57	29±0.47	28±0.57	27±0.57	26±1.15	26±0.47	25±0.57
[Co(MBA)$_2$.Cl$_2$]	15±0.47	17±0.57	16±1.15	18±0.57	17±0.47	16±0.57	16±0.47	19±0.57
[Ni(MBA)$_2$.Cl$_2$]	11±1.52	11±1.15	12±0.57	13±1.15	12±0.47	13±1.15	12±1.15	14±0.47
[Cu(MBA)$_2$.Cl$_2$]	14±1.15	12±0.47	13±1.15	13±0.47	14±1.52	15±0.47	14±1.15	15±0.47
[Zn(MBA)$_2$.Cl$_2$]	19±1.52	18±1.15	20±0.57	21±1.15	20±0.47	22±1.15	21±1.15	23±0.47
Std 2	10±1.52	09±1.15	09±0.57	08±1.15	08±0.47	07±1.15	06±1.15	08±0.47

*Std 2: Flucanazole.

*Each value is expressed as mean ± SD of three replicates for the zone of inhibition.

3.11.2. Antioxidant activity.

As an increasingly popular tool for the assessment of antioxidant potency, the DPPH radical scavenging activity test is regarded as a standard assay for the exploration of the oxidative potential of various metal complexes. The stable organic radical 1,1-Diphenyl-2-picrylhydrazyl (DPPH) emits a dark purple color because of the presence of free radical DPPH with maximum absorption at 517nm. Any compound that releases hydrogen atoms or electrons will undoubtedly react with this radical, switching its color from purple to yellow. Due to the compound's ability to discharge hydrogen, the extent of color change is a good indication of its scavenging capability. Assays were performed to assess the antioxidant activity of MBA and its metal complexes at various concentrations (20–100 g/ml) compared with BHT used as a reference. The outcomes are entered in Table 12 and delineated in Figure 18. The method described in the procedure section determined the antioxidant activity of MBA and its metal compounds.

Table 12. Antioxidant activity of MBA and its metal complexes.

Compounds	% of Scavenging activity (concentrations in μg/mL)				
	20	40	60	80	100
MBA	20.52±0.36	32.00±0.23	48.12±0.39	56.02±0.15	64.02±0.13
[Co(MBA)$_2$.Cl$_2$]	35.45±0.71	49.87±0.37	70.14±0.12	78.03±0.11	93.37±0.25
[Ni(MBA)$_2$.Cl$_2$]	39.16±0.20	56.87±0.24	71.35±0.38	80.12±0.46	94.15±0.28
[Cu(MBA)$_2$.Cl$_2$]	30.79±0.24	44.96±0.22	65.26±0.30	70.86±0.22	89.91±0.29
[Zn(MBA)$_2$.Cl$_2$]	24.65±0.31	38.79±0.37	60.12±0.29	65.45±0.32	81.17±0.54
Std	44.06±0.56	59.15±0.50	78.65±0.31	83.07±0.44	98.26±0.58

*Std : Butylated hydroxytoluene.

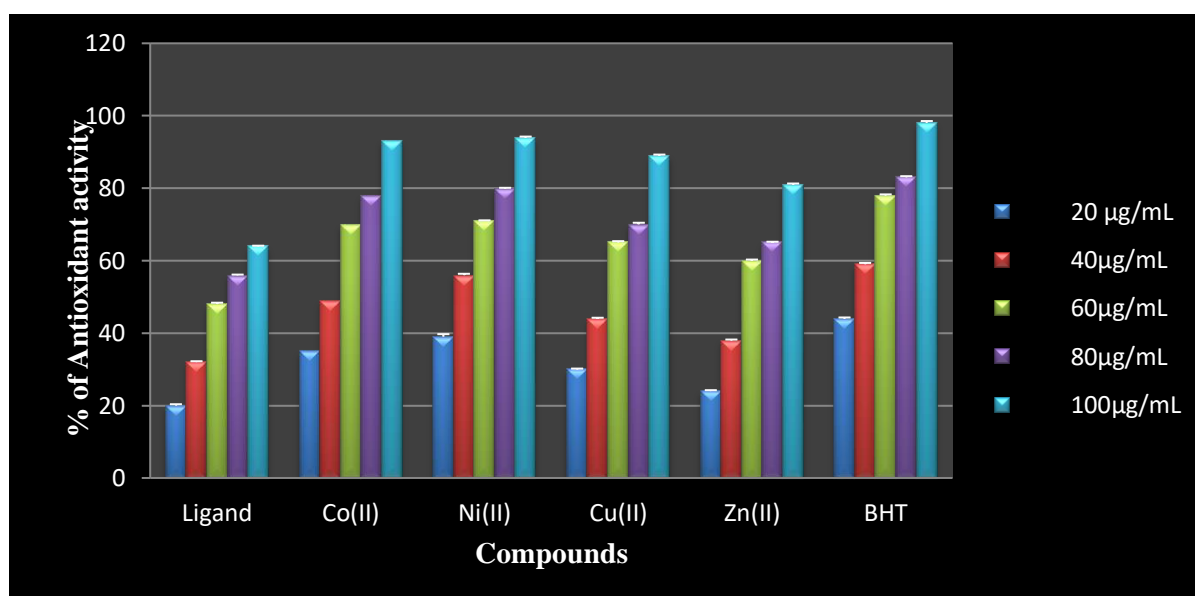*Each value is expressed as mean ± SD of three replicates for the zone of inhibition.

Figure 18. Antioxidant activity of Ligand MBA and its metal complexes.

It was perceived from the antioxidant data that the metallic complexes had higher scavenging effects than that of MBA but were least potent than BHT. We observed that the radical scavenging activity of metallic complexes and the standard increased proportionally to the dose and chelation with transition metal ions, significantly enhancing MBA's antioxidant ability. Furthermore, Co(II) and Ni(II) complexes were exposed to stronger DPPH scavenging activity with high scavenging rates(35.45-93.37 & 39.16-94.15). All the other complexes were

moderately active compared to MBA. On the whole, oxidizing potentials of the samples are related to the presence of compounds that break the free radical chain through hydrogen atom donation. As such, the results of this study have implications for the use of synthesized compounds in treating oxidative stress-induced pathological diseases [40].

3.11.3. Molecular docking studies.

To unravel the binding interactions between MBA and its coordinated compounds, adocking study was done using anticancer receptor PDB id:2A91 with Actinoin utilized as a reference. Our approach to evaluating the stability of best-docked poses involved measuring the hydrogen bonding interactions of proteins with complexes revealing the inclusion of amino acids in hydrogen bond formation.

According to the factors discussed in the preceding paragraph, the Ni(II) and Cu(II) compounds possess minimal docking scores of -307.49 and -299.81 kcal/mol compared with the reference (-235.99kcal/mol) and MBA (-220.16 kcal/mol). Diverse binding interactions (hydrogen bonding, Pi-Pi, Pi-Alkyl, Alkyl) with unique amino acids in the receptor enzyme made metal complexes a brilliant anticancer receptor binding species. The Ni(II) and Cu(II) compounds interact (Pi-Pi, Pi-Alkyl, Alkyl) with active sites of 2A91 receptor's amino acids are GLU40, LEU41, THR42, TYR43, LEU44, PRO45, THR46, ASN47, ALA48, PHE87, GLU88, ASP89, ASN90, TYR91, ALA92, LEU93, TRP500, GLY501, PRO502, LEU86, PHE87, GLU88 andASP89, ASN90, TYR91, ALA92, ASP510. The docking values of MBA and its coordinated compounds are placed in Table13, and 2D and 3D images of metal complexes bound to receptor 2A91 are pictured in Figure 19 (a)-(d).

Table 13. Molecular docking score of MBA & its metal complexes.

Compounds	Receptor	E (kcal mol^{-1})
MBA	2A91	-220.16
[Co(MBA)$_2$.Cl$_2$]	2A91	-291.17
[Ni(MBA)$_2$.Cl$_2$]	2A91	-307.59
[Cu(MBA)$_2$.Cl$_2$]	2A91	-299.81
[Zn(MBA)$_2$.Cl$_2$]	2A91	-290.57
Actinoin (STD)	2A91	-235.99
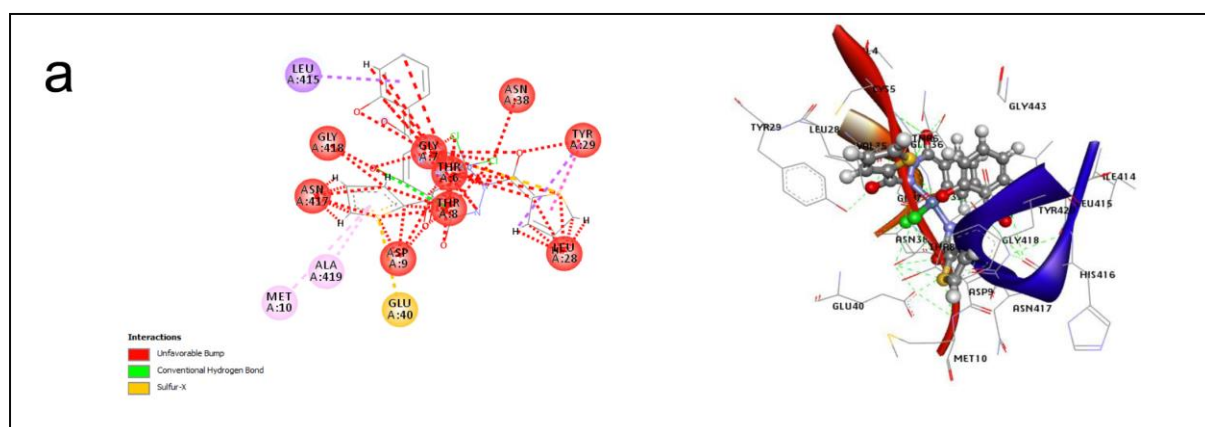
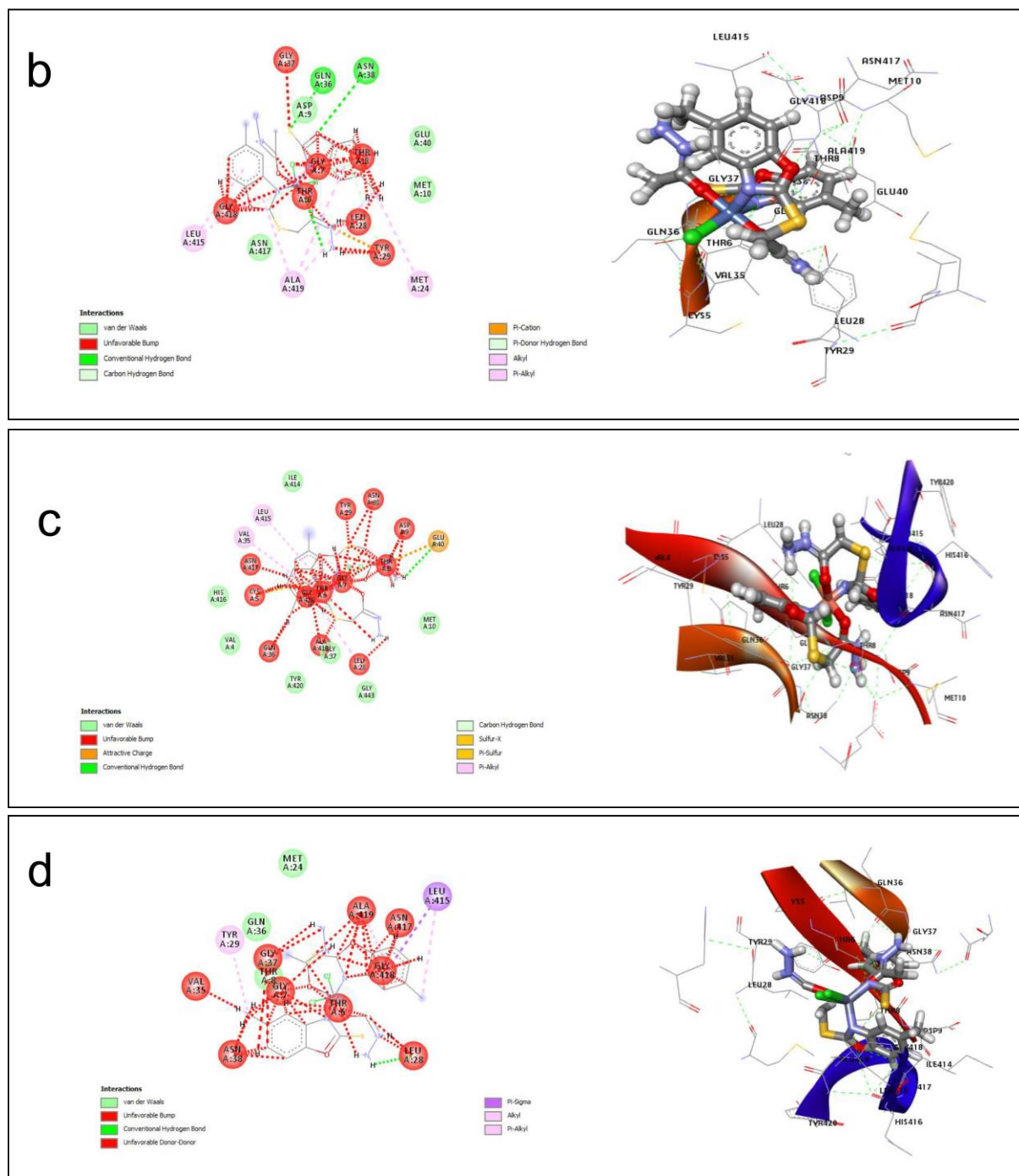**Figure 19.** 2-D and 3-D binding orientation of metal complexes with receptor 2A91 **(a)** Co(II); **(b)** Ni(II); **(c)** Cu(II); **(d)** Zn(II).

3.11.4. Cytotoxic studies.

Discovering metal-based anticancer drugs is one of the highest priorities in pharmaceutical research [41]. MBA and its transition metal complexes were detected for their *invitro* cytotoxicity against selected human cancer cell lines of breast adenocarcinoma (MCF-7) and cervical carcinoma (HeLa) using 3-(4,5-dimethythiazol-2-yl)-2,5-diphenyl tetrazolium bromide(MTT) assay. Untreated cells functioned as control, and cancer cells were treated with varying concentrations of ligand and metal complexes (400, 200, 100, 50, 25, 12.5 g/ml). The screening results are summed up in Table 14 and graphically addressed in Figure 20. The data gathered revealed that the complexes had a dose-dependent inhibitory impact on the proliferation of MCF-7and HeLa cell lines.

Accordingly, the high inhibitory score of the metal complexes against uncoordinated ligand MBA implies that the ligand and metallic ions coordinate synergistically. At the lowermost concentration (12.5 µg/ml), Ni(II) and Cu(II) compounds showcased an appreciative inhibition score of 50% and 44% for MCF-7 cells, whereas, for HeLa cells, the same compounds demonstrated 63% and 61% viability scores at the least concentration (12.5µg/ml). In a later test, Co(II) complex showed appealing cytotoxicity of 42% and 59% for MCF-7 and HeLa cell strains at 12.5µg/ ml, and also the viability scores of Zn(II) complex outlined the satisfactory results regarding the inhibition of proliferation of both MCF-7 and HeLa cells.

Additionally, IC$_{50}$ (the concentration of the compound in µg/ml that hinders proliferation of the cells by 50% compared to the standard Paclitaxel) values of MBA and its metal complexes were also calculated, and the results are entered in Table 15 and depicted in Figure 21. It was noticed that Ni(II) complex evidenced superior cytotoxic activity with IC$_{50}$ values of 3.68 and 5.10 µg/ml for MCF-7 and HeLa cell lines compared to the ligand and other synthesized metal complexes. Overall the cytotoxicity of MBA and its metallic complexes illuminates the significance of the coordination process on the biological properties. In Supplementary Information (Figure S2 and Figure S3), we present microscopical images of MCF-7 and HeLa cell lines after treatment with synthesized ligand and its metal complexes compared with negative control (untreated cells).

Table 14. *In vitro* cytotoxicity of ligand MBA and its metal complexes against human cancer cell lines.

Compound	MCF-7						HeLa					
	400	200	100	50	25	12.5	00	00	00	0	5	2.5
MBA	20±0.47	22±0.11	25±1.25	27±0.57	31±0.22	38±0.11	5±1.52	8±1.15	0±1.15	2±1.15	0±0.57	2±0.47
[Co(MBA)₂.Cl₂]	23±1.15	25±1.52	28±0.19	30±0.47	35±0.65	42±1.74	5±1.15	7±0.22	9±0.14	0±0.14	7±0.22	9±1.15
[Ni(MBA)₂.Cl₂]	27±0.90	29±0.13	33±1.15	38±0.47	44±1.24	50±0.33	9±0.57	0±1.15	4±0.47	5±0.13	0±1.15	3±0.57
[Cu(MBA)₂.Cl₂]	24±0.57	27±1.15	29±0.22	35±0.58	38±0.18	44±1.25	7±0.47	9±1.15	3±0.47	1±0.16	8±0.22	1±0.57
[Zn(MBA)₂.Cl₂]	22±0.65	24±0.33	27±1.15	29±1.52	34±0.47	40±0.17	1±0.47	4±0.22	5±0.57	9±1.74	5±1.52	8±0.47
Negative Control	100											

*Each value is expressed as the mean ± SD of three replicates for the zone of inhibition.
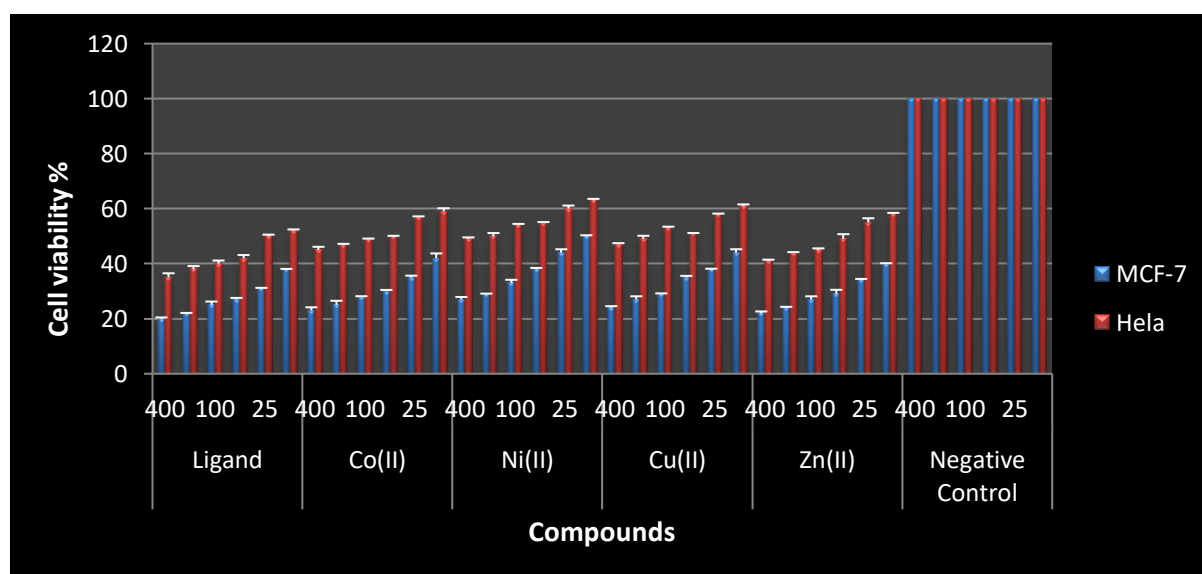

Figure 20. Cytotoxic efficiency of ligand MBA and its transition metal complexes.

Table 15. IC_{50} values of Ligand MBA and its metal complexes against MCF-7 and HeLa cell lines.

Compounds	Cell line	IC_{50} (µg/mL)
MBA	MCF-7	13.28±0.65
	HeLa	18.63±0.58
[Co(MBA)$_2$.Cl$_2$]	MCF-7	8.37±0.22
	HeLa	9.45±1.15
[Ni(MBA)$_2$.Cl$_2$]	MCF-7	3.68±1.52
	HeLa	5.10±1.74
[Cu(MBA)$_2$.Cl$_2$]	MCF-7	6.57±1.25
	HeLa	7.96±0.11
[Zn(MBA)$_2$.Cl$_2$]	MCF-7	10.68±0.58
	HeLa	11.66±1.15
Paclitaxel	MCF-7	0.32±0.65
(Positive control)	HeLa	0.22±1.52

Figure 21. IC_{50} values of ligand and its transition metal complexes against cancer cell line compared with Paclitaxel (Positive control).

4. Conclusions

A novel ligand 2-[(5-methyl-1,3-benzoxazol-2-yl)sulfanyl]acetohydrazide (MBA) has been synthesized in the existing work to produce biologically active Co(II), Ni(II), Cu(II), and Zn(II) complexes which have been assessed by a range of physicochemical and spectral approaches. We were able to elucidate the structure of MBA and its metallic compounds by varied analytical methodologies. The collected data supports the hypothesis that the synthesized ligand would lead to forming a bidentate ligand with octahedral geometry ascribed to all metal complexes. A wide range of glucose and H_2O_2 concentrations were used to examine the electrocatalytic activity of the Co(II)MBA complex. The modified electrode showcased noteworthy results like high sensitivity, LOD, wide concentration range, stability, and reproducibility.

Investigation of antimicrobial, antioxidative, and cytotoxic efficacies was performed for the uncoordinated ligand and its metal complexes. Results from the recorded antimicrobial tests demonstrated that Ni(II) and Cu(II) complexes were more powerful biocompounds than the rest of the metal complexes. In contrast, Co(II) and Ni(II) complexes exhibited commendable radical scavenging activities. The results of molecular docking studies aroused our interest in studying the cytotoxic activity of the ligand and its coordinated compounds

against two cell lines, in which it has been proven that contrary to uncoordinated ligands, all metal complexes had praiseworthy cytotoxicity.

Funding

Acknowledgments

Conflicts of Interest

The authors declare no conflict of interest.

References

1. Andris, E.; Kevin, A. K. Evaluation of metal-based antimicrobial compounds for the treatment of bacterial pathogens. *Journal of Medical Microbiology* **2021**, *70*, 001363, https://doi.org/10.1099/jmm.0.001363.
2. Oulmidi, A.; Radi, S.; Idir, A.; Zyad, A.; Kabach, I.; Nhiri, M.; Robeyns, K.; Rotaru, A.; Garcia, Y. Synthesis and cytotoxicity against tumor cells of pincer N-heterocyclic ligands and their transition metal complexes. *RSC Adv* **2021**, *11*, 34742-34753, https://doi.org/10.1039/D1RA05918A.
3. Valente, A.; Podolski-Renic, A.; Poetsch, I.; Filipovic, N.; Lopez, O.; Turel, I.; Heffeter, P. Metal- and metalloid-based compounds to target and reverse cancer multidrug resistance. *Drug Resistance Updates* **2021**, *58,* 100778, https://doi.org/10.1016/j.drup.2021.100778.
4. Madhumitha, S.RM.; Mahrukh, M.; Chundru, Sowmya.; Ravichandran, S. The importance of transition metalsas drug. *International Journal of Clinical Biochemistry and Research* **2022**, *9*, 1-3,https://doi.org/10.18231/j.ijcbr.2022.001.
5. Tesauro, D. Metal Complexes in Diagnosis and Therapy. *Int. J. Mol. Sci* **2022**, *23*, 4377, https://doi.org/10.3390/ijms23084377.
6. Kamal, U.; Naim, M.J.; Kumar, A.; Biological Potential Of Benzoxazole Derivatives: An Updated Review. *Asian J Pharm Clin Res* **2020**, *13,* 28-41, http://doi.org/10.22159/ajpcr.2020.v13i8.37958.
7. Cheerala, V. S. K.; Ghanta, P.; Neelakantan, S. C. Design, synthesis and in silico screening of benzoxazole–thiazolidinone hybrids as potential inhibitors of SARS-CoV-2 proteases. *RSC Adv* **2021**, *11,* 39328-39342, https://doi.org/10.1039/D1RA07504G.
8. Kaur, A; Pathak, D.P.; Sharma.V.; Wakode, S. Synthesis, biological evaluation and docking study of a new series of di-substituted benzoxazole derivatives as selective COX-2 inhibitors and anti-inflammatory agents. *Bioorg Med Chem* **2018**, *26,* 891-902, https://doi.org/10.1016/j.bmc.2018.01.007.
9. Shivani, B. Recent Advances in Synthesis of Benzoxazole. *Mini-reviews in Organic Chemistry* **2021**, *18*, 383-397, https://doi.org/10.2174/1570193X17999200706010457.
10. Rashed, M.A.; Faisal, M.; Farid, A.H.; Jalalah, M.; Mabkhoot, A.; Alsareii, S.A. A Highly Efficient Nonenzymatic Hydrogen Peroxide Electrochemical Sensor Using Mesoporous Carbon Doped ZnO Nanocomposite. *Journal of The Electrochemical Society* **2021**, *168,* 027512, https://doi.org/10.1149/1945-7111/abe44b.
11. Franco, F.F.; Hogg, R.A.; Manjakkal, L. Cu2O-Based Electrochemical Biosensor for Non-Invasive and Portable Glucose Detection. *Biosensors* **2022**, *12*, 174, https://doi.org/10.3390/bios12030174.

12. Jayaprakasha,G.K.; Kumara Swamy, B.E; Sharma, S.C.; Santoyo-Flores,J.J. Analyzing electron transfer properties of ferrocene in gasoline by cyclic voltammetry and theoretical methods. *Microchemical Journal* **2020,***158,* 105116,https://doi.org/10.1016/j.microc.2020.105116.

13. Jayaprakash, G.K.; Kumara Swamy, B.E.; Rajendrachari, S.; Sharma, S.C.; Flores-Moreno, R. Dual descriptor analysis of cetylpyridinium modified carbon paste electrodes for ascorbic acid sensing applications. *Journal of Molecular Liquids* **2021**, *334,* 116348, https://doi.org/10.1016/j.molliq.2021.116348.

14. Mohammed, O.A.; Dahham, O.S. Synthesis, Characterization, and Study of Antibacterial Activity of Some New Formazan Dyes Derivatives, Derived from 2-Mercapto Benzoxazole. *IOP Conf. Series: Materials Science and Engineering* **2018**, *454*, 012015, https://doi.org/10.1088/1757-899X/454/1/012015.

15. Kakkar, S.; Tahlna, S.; Lim, S.M.; Ramasamy, K.; Mani, V.; Shah, S.A.A.; Narasimhan, B. Benzoxazole derivatives: design, synthesis and biological evaluation. *Chem Cent J* **2018,** *12,* 92, https://doi.org/10.1186/s13065-018-0459-5.

16. Lubna, A.; Moinuddin, K.M.H.; Vagdevi, H.M.; Malathesh, P.; Mohammed, S.R.; Mussuvir P.K.M. Investigation on Co(II), Ni(II), Cu(II), and Zn(II) complexes derived from novel *N'*-(3-hydroxybenzoyl) thiophene-2-carbohydrazide:structural characterization, electrochemical detection of biomolecules, molecular docking, and biological evaluation. *Emergent Materials* **2021,** *23*, https://doi.org/10.1007/s42247-021-00312-4.

17. Hasan, M.M.; Ahsan, H.M.; Saha, P.; Naime, J.; Das, A.K.; Asraf, M.A.; Islam, A.B.M.N. Antioxidant, antibacterial and electrochemical activity of (E)-N-(4 (dimethylamino) benzylidene)-4H-1,2,4-triazol-4-amine ligand and their transition metal complexes. *Results in Chemistry* **2021**, *3,* 100115, https://doi.org/10.1016/j.rechem.2021.100115.

18. Shafeeulla, M.R.; Krishnamurthy, G.; Bhojyanaik, H.S.; Manjuraj, T. Synthesis, Cytotoxicity, and Molecular Docking Study of Complexes Containing Thiazole Moiety. *JOTCSA* **2017**, *4*, 787-810, https://doi.org/10.18596/jotcsa.309261.

19. Shafeeulla, M.R.; Krishnamurthy, G.; Bhojyanaik, H.S.; Shivarudrappa, H.P.; Shiralgi, Y. Spectral thermal cytotoxic and molecular docking studies of N'-2-hydroxybenzoyl; pyridine-4-carbohydrazide its complexes. *Beni-Suef Univ J Basic Appl Sci* **2017** *,6,* 332-344,https://doi.org/10.1016/j.bjbas.2017.06.001.

20. Kumbar, V.M.; Peram, M.R.; Kugaji, M.S.; Shah, T.; Patil, S.P.; Muddapur, U.M.; Bhat, K.G. Effect of curcumin on growth, biofilm formation and virulence factor gene expression of Porphyromonas gingivalis. *Odontology* **2021***, 109,* 18-28, https://doi.org/10.1007/s10266-020-00514-y.

21. Samota, M.K.; Seth, G. Synthesis, Characterization, and Antimicrobial Activity of Palladium(II) and Platinum(II) Complexes with 2-Substituted Benzoxazole Ligands. *Heteroatom Chem* **2010**, *21*, 44–50, https://doi.org/10.1002/hc.20578.

22. Jie, J.; Xiaoliang, T.; Wei, D.; Huihui, Z.; Weisheng, L.; Chenxuan, W.; Jiangrong, Z. Synthesis and characterization of the ligand based on benzoxazole and its transition metal complexes: DNA-binding and antitumor activity. *Journal of Inorganic Biochemistry* **2010**, *104*, 583–591, https://doi.org/10.1016/j.jinorgbio.2010.01.011.

23. Mangamamba, T.; Ganorkar, M.C.; Swarnabala, G. Characterization of Complexes Synthesized Using Schiff Base Ligands and Their Screening for Toxicity Two Fungal and One Bacterial Species on Rice Pathogens. *International J Inorganic Chem* **2014***,* 736538, http://doi.org/10.1155/2014/736538*.

24. Matada, M.N.; Jathi, K. Pyrazole-based azo-metal(II) complexes as potential bioactive agents: synthesis, characterization, antimicrobial, anti-tuberculosis, and DNA interaction studies. *Journal of Coordination Chemistry* **2019**, *72*, 1994-2014, https://doi.org/10.1080/00958972.2019.1630613.

25. Al-jibouri, M.N.; Jawad, W.A.; Balakit, A.A.; Obies, M. Synthesis, Characterization (Theoretical and Biological Study) of Some Transition Metal Complexes with New Schiff Base Derived from 1,2,4-triazole. *Egypt. J. Chem* **2021**, *64*, 5227 – 5239, https://doi.org/10.21608/ejchem.2021.71885.3580.

26. Abulnabi, Z.A.; Al-doghachi, F.A.J.; Abdulsahib, H.T. Synthesis, Characterization and Thermogravimetric Study of Some Metal Complexes of Selenazone Ligand Nanoparticles Analogue of Dithizone. *Indones. J. Chem* **2021**, *21*, 1231-1243, https://doi.org/10.22146/ijc.65763.

27. Gaber, A.; Belal, A.A.M.; El-Deen, I.M.; Hassan, N.; Zakaria, R.; Alsanie,W.F.; Naglah, M.A.; Refat, M.S. Synthesis, Spectroscopic Characterization, and Biological Activities of New Binuclear Co(II), Ni(II), Cu(II), and Zn(II) Diimine Complexes. Crystals **2021**, *11*, 300, https://doi.org/10.3390/cryst11030300.

28. Sun, A.; Zhenga, J.; Sheng, Q. A highly sensitive non-enzymatic glucose sensor based on nickel and multi-walled carbon nanotubes nanohybrid films fabricated by one-step co-electrodeposition in ionic liquids. *Electrochimica Acta* **2012**, *65*, 64–69, http://doi.org/10.1016/j.electacta.2012.01.007.

29. Shan, C.S.; Yang, H.F.; Han, D.X.; Zhang, Q.X.; Ivaska, A.; Niu, L. Graphene/AuNPs/chitosan nanocomposites film for glucose biosensing. *Biosens Bioelectron* **2010**, *25*, 1070−1074, https://doi.org/10.1016/j.bios.2009.09.024.

30. Jia, X.; Hu, G.; Nitze, F.; Barzegar, H.R.; Sharifi, T.; Tai, C.W. Synthesis of Palladium/Helical Carbon Nanofiber Hybrid Nanostructures and Their Application for Hydrogen Peroxide and Glucose Detection. *ACS Appl Mater Interfaces* **2013***, 5*, 12017−12022, https://doi.org/10.1021/am4037383.

31. Ekanayake, E.M.I.M.; Preethichandra, D.M.G.; Kaneto, K. Polypyrrole nanotube array sensor for enhanced adsorption of glucose oxidase in glucose biosensors. *Biosensors and Bioelectronics* **2007**, *23*, 107–113, https://doi.org/10.1016/j.bios.2007.03.022.

32. Mahmoudian, M.R.; Basirun, W.J.; Woi, P.M.; Sookhakian, M.; Yousefi, R.; Ghadimi, H.; Alias, Y. Synthesis and characterization of Co_3O_4 ultra-nanosheets and Co_3O_4 ultra-nanosheet-$Ni(OH)_2$ as non-enzymatic electrochemical sensors for glucose detection. *Mater Sci Eng C* **2016** *59*, 500–508, https://doi.org/10.1016/j.msec.2015.10.055.

33. Gupta, S.; Smith, T.; Banaszak, A.; Boeckl, J. Graphene Quantum Dots Electrochemistry and Development of Ultrasensitive Enzymatic Glucose Sensor. *MRS Advances* **2018**, *3*, 831-847, https://doi.org/10.1557/adv.2018.324.

34. Li, L.; Du, Z.; Liu, S.; Hao, Q.; Wang, Y.; Li, Q.; Wang, T. A novel nonenzymatic hydrogen peroxide sensor based on MnO2/graphene oxide nanocomposite. *Talanta* **2010**, *82*, 1637-1641, http://doi.org/10.1016/j.talanta.2010.07.020.

35. Kacar, C.; Dalkiran, B.; Erden, P.E.; Kilic, E. An amperometric hydrogen peroxide biosensor based on Co_3O_4 nanoparticles and multiwalled carbon nanotube modified glassy carbon electrode. *Appl Surf Sci* **2014**, *311*, 139-146, https://doi.org/10.1016/j.apsusc.2014.05.028.

36. Jirimali, H.D.; Saravanakumar, D.; Shin, W. Chitosan-Cu-salen/Carbon Nano-Composite Based Electrode for the Enzyme-less Electrochemical Sensing of Hydrogen Peroxide. *J Electrochem Sci Technol* **2018,** *9***,** 169-175,https://doi.org/10.5229/JECST.2018.9.3.169.

37. Maduraiveeran, G.; Kundu, M.; Sasidharan, M. Electrochemical detection of hydrogen peroxide based on silver nanoparticles via amplified electron transfer process. *J Mater Sci* **2018**, *53*, 8328, https://doi.org/10.1007/s10853-018-2141-7.

38. Ujjain, S.K.; Ahuja, P.; Roy, M.; Singh, S.K.; Sharma, R.K.; Das, M. Nanoceria based electrochemical sensor for hydrogen peroxide detection. *Biointerphases* **2014**, *9,* 03101, http://doi.org/10.1116/1.4890473.

39. Kadhum, A.A.H.; Mohamad, A.B.; Al-Amiery, A.A.; Takriff, M.S. Antimicrobial and Antioxidant Activities of New Metal Complexes Derived from 3-Aminocoumarin. *Molecules* **2011**, *16*, 6969-6984, http://doi.org/10.3390/molecules16086969.

40. Ejidike, I.P.; Ajibade, P.A. Synthesis, Characterization, Antioxidant and Antibacterial Studies of Some Metal(II) Complexes of Tetradentate Schiff Base Ligand: (4E)-4-[(2-{(E)-[1-(2,4-Dihydroxyphenyl)ethylidene]amino}ethyl) imino]pentan-2-one. *Bioinorg Chem Appl* **2015**, *8*, 1-9, http://dx.doi.org/10.1155/2015/890734.

41. Frezza, M.; Hindo, S.; Chen, D.; Davenport, A.; Schmitt, S.; Tomco, D.; Dou, Q.P. Novel metals and metal complexes as platforms for cancer therapy.*Current pharmaceutical design* **2010**, *16*, 1813–1825,https://doi.org/10.2174/138161210791209009.
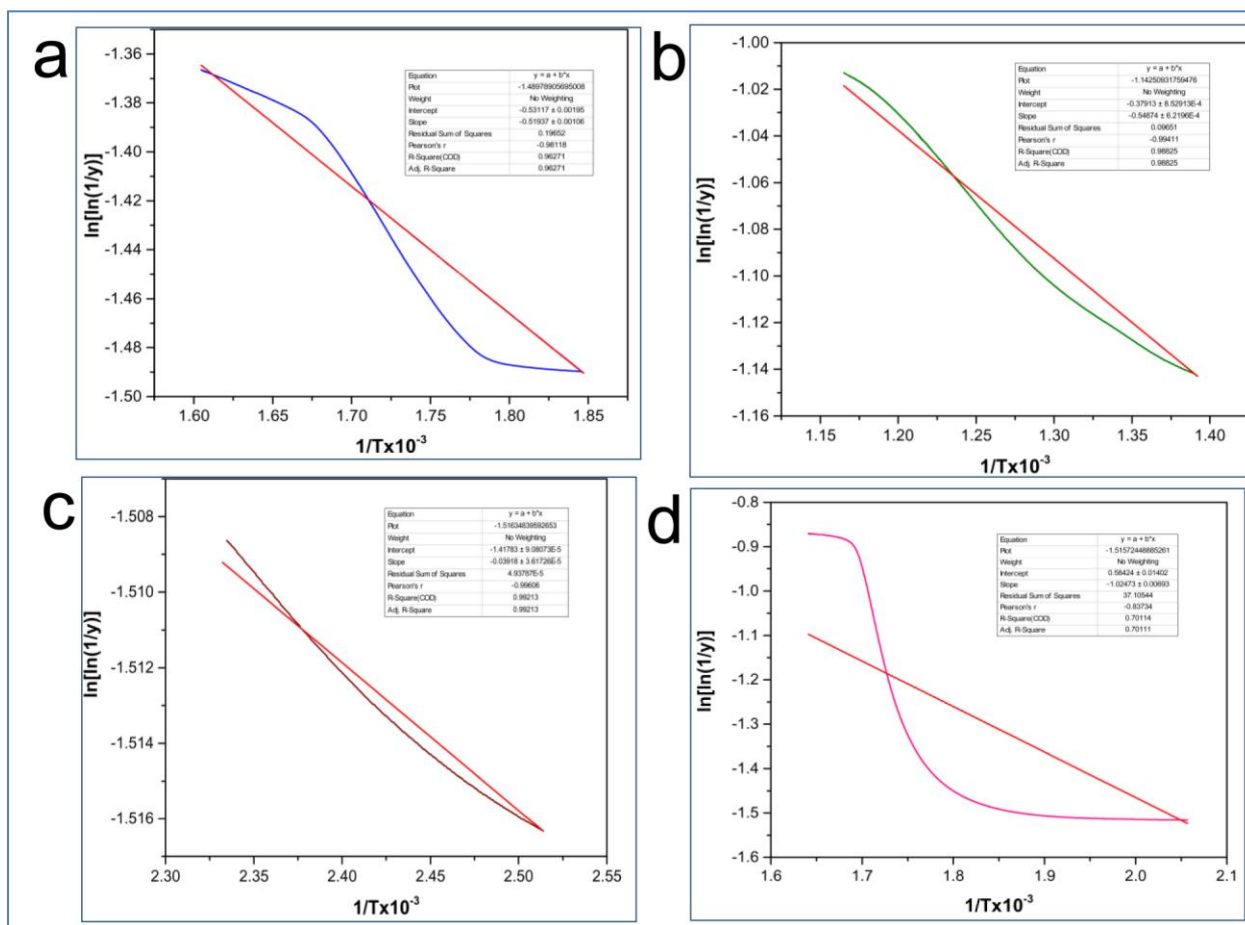
Supplementary materials

Figure S1. Linear fit graphs of (a) Co(II) complex (b) Ni(II) complex (c) Cu(II) complex (d) Zn(II) complex.
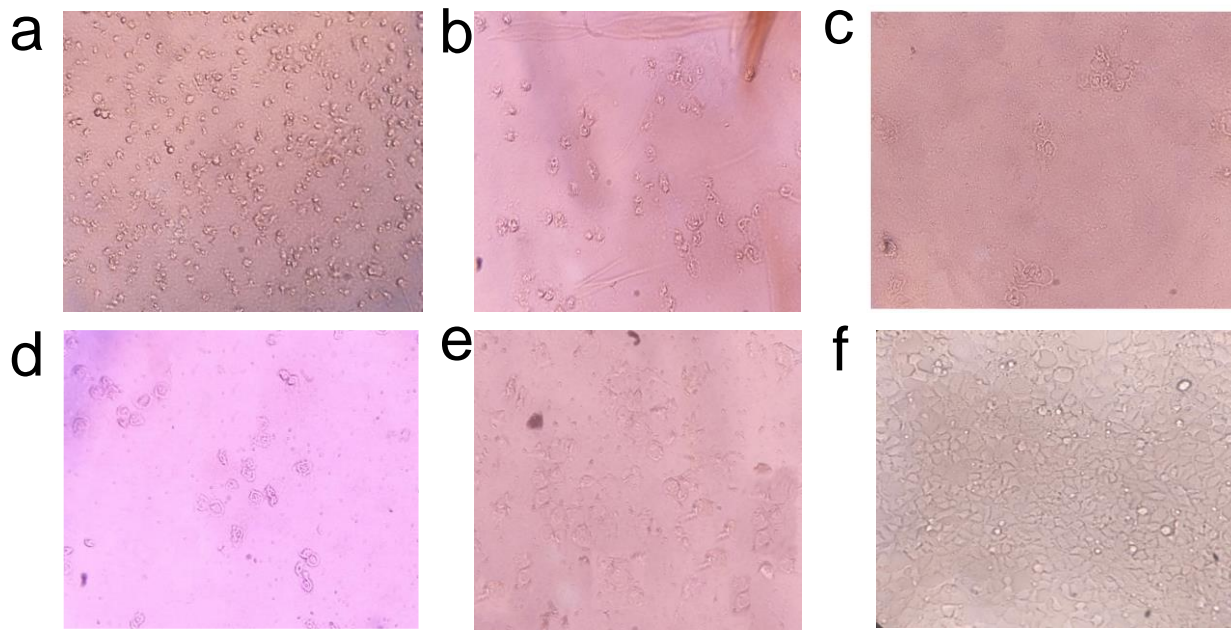

Figure S 2. Effect of (a) Ligand (b) Co(II) complex (c) Ni(II) complex (d) Cu(II) complex (e) Zn(II) complex (d) Negative control on cell viability of MCF-7 cells at the concentration range 25µg/ml (binocular research microscope objective at 200x magnification).
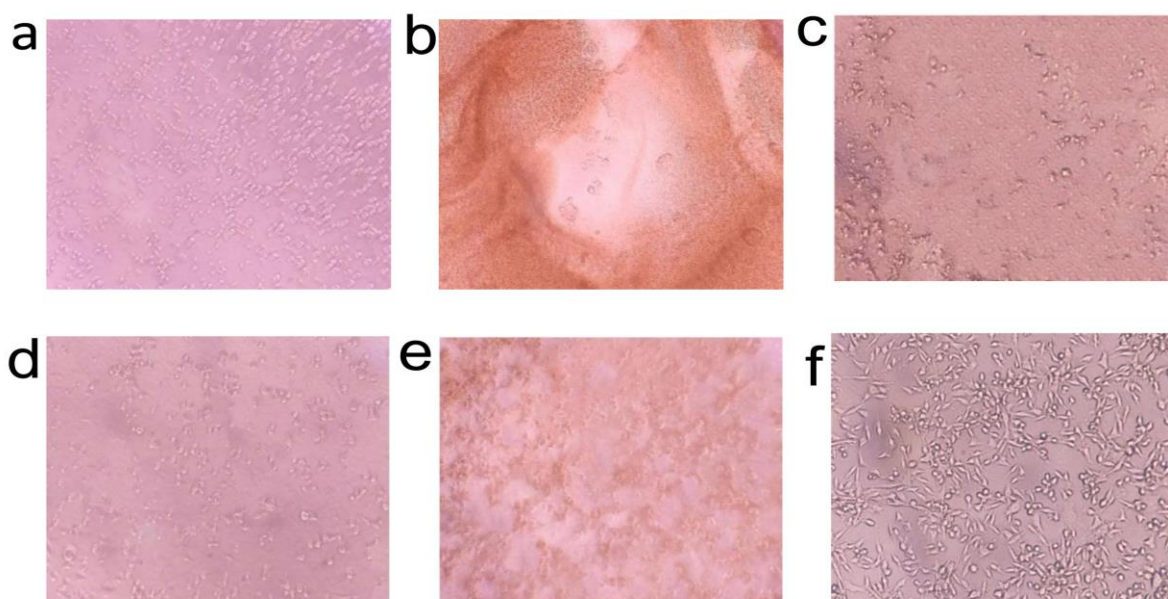
Figure S3. Effect of (a) Ligand (b) Co(II) complex (c) Ni(II) complex (d) Cu(II) complex (e) Zn(II) complex (d) Negative control on cell viability of HeLa cells at the concentration range 25µg/ml (binocular research microscope objective at 200x magnification).